
U-HNO: A U-shaped Hybrid Neural Operator with Sparse-Point Adaptive Routing for Non-stationary PDE Dynamics

Yingzhe Ma¹ Xiao Yang¹ Yuxin Xie² Zihan Xiong¹ Jinliang Liu¹

¹University of Electronic Science and Technology of China ²Peking University

Abstract

Solutions to many partial differential equations (PDEs) display coexisting smooth global transport and localized sharp features within a single trajectory: shock fronts, thin interfaces, and concentrated high-frequency content sit on top of slowly varying backgrounds. This poses a fundamental challenge for neural operators: Fourier-based architectures mix nonlocal interactions efficiently through frequency-domain parameterization but tend to under-resolve localized non-smooth features, whereas spatially local architectures recover fine detail at the cost of long-range propagation and rollout stability. Existing hybrid operators paper over this tension with a fixed, spatially uniform fusion—additive concatenation or a single global gate—that forces the same trade-off everywhere in the field.

We propose U-HNO, a U-shaped hybrid neural operator whose central design is Sparse-Point Adaptive Routing (SPAR): at every spatial location, a per-pixel hard mask selects whether the global Fourier branch or the local multi-scale Gaussian branch should dominate, and the sparsity ratio itself is a function of the local contrast of the routing signal, so smooth regions and shock-aligned regions receive different mixtures of global and local computation. SPAR is embedded in a hierarchical encoder–bottleneck–decoder backbone with skip connections so that the dual branches and the gate operate at every resolution. Training combines pointwise supervision with a finite-difference H^1 gradient term and a band-wise spectral consistency regularizer, jointly targeting field accuracy, gradient fidelity, and frequency stability across rollout horizons.

Across a heterogeneous benchmark suite spanning 1D Burgers, Kuramoto–Sivashinsky, and KdV equations, 2D advection, Allen–Cahn, Navier–Stokes, and Darcy flow, as well as 3D compressible Navier–Stokes at transonic Mach number from PDEBench, U-HNO achieves state-of-the-art rollout accuracy on the majority of tasks in both relative L^2 and gradient-aware H^1 metrics, with the largest gains on problems dominated by sharp localized features such as 1D Burgers and the transonic 3D case. An ablation across nine variants shows that removing any single component—the hierarchical backbone, the dual-branch design, the contrast-adaptive SPAR gate, or the structured loss—substantially degrades rollout error, indicating that the gains do not concentrate in any one ingredient.

1 Introduction

Operator learning approximates mappings between infinite-dimensional function spaces and provides fast surrogates for repeated PDE simulation, inverse problems, and design [12, 10]. Fourier neural operators (FNO) [12] are popular because frequency-domain parameterization mixes nonlocal interactions efficiently and generalizes across resolutions. Their weakness is the flip side of this strength: PDE solutions are rarely spectrally uniform. Smooth large-scale transport coexists with sharp transitions, boundary layers, shocks, and fine interfaces. Networks are biased toward low frequencies [20], and a flat global mode budget allocates the same spectral capacity everywhere irrespective of local frequency content. Spatially local operators [13, 19, 3] attack the bias from the opposite side, improving local detail at the cost of efficient long-range propagation. The gap is a neural operator that preserves *both* local spatial fidelity and global spectral coherence, which is most acute for non-stationary spectral fields where the dominant frequency varies in space, time, and initial condition.

Approach. We introduce **U-HNO**. A multi-scale Gaussian local branch and a Fourier branch run in parallel inside a U-shaped backbone with skip connections [21], exposing the hybrid at every resolution. A Sparse-Point Adaptive Routing (SPAR) gate, drawing on content-adaptive sparse sampling [9] and sparsely-gated MoEs [25], emits a per-pixel hard choice between the two branch outputs in the forward pass and masks the dominant output-gradient at that location to the chosen branch in the backward pass; both branches are evaluated everywhere, so SPAR is a representational dispatcher rather than a compute-saving mechanism. Training combines single-step MSE, a finite-difference gradient term, and a cross-branch consistency regularizer.

Why this inductive bias. Figure 1 visualizes three diagnostics. (a) Frequency content varies sharply within a single Burgers trajectory—mid/high-frequency energy concentrates near shocks while ambient regions stay low-frequency, so uniform spectral truncation must trade off one regime against another. (b) Inside a flat additive FNO+local hybrid, the layer-wise cosine angle between $\nabla_{\theta_F} \mathcal{L}$ and $\nabla_{\theta_G} \mathcal{L}$ on NS (App. A.5) concentrates at 90° , indicating near-orthogonal training signals. (c) Pure spectral baselines accumulate high-frequency drift under long rollout that pointwise MSE does not suppress. Panels (d–f) show U-HNO mirror diagnostics on the same tasks: all three pathologies are attenuated. These motivate (i) a multi-resolution U-shape, (ii) per-pixel commitment of SPAR over additive fusion, and (iii) a structured loss penalizing gradient and cross-branch divergence.

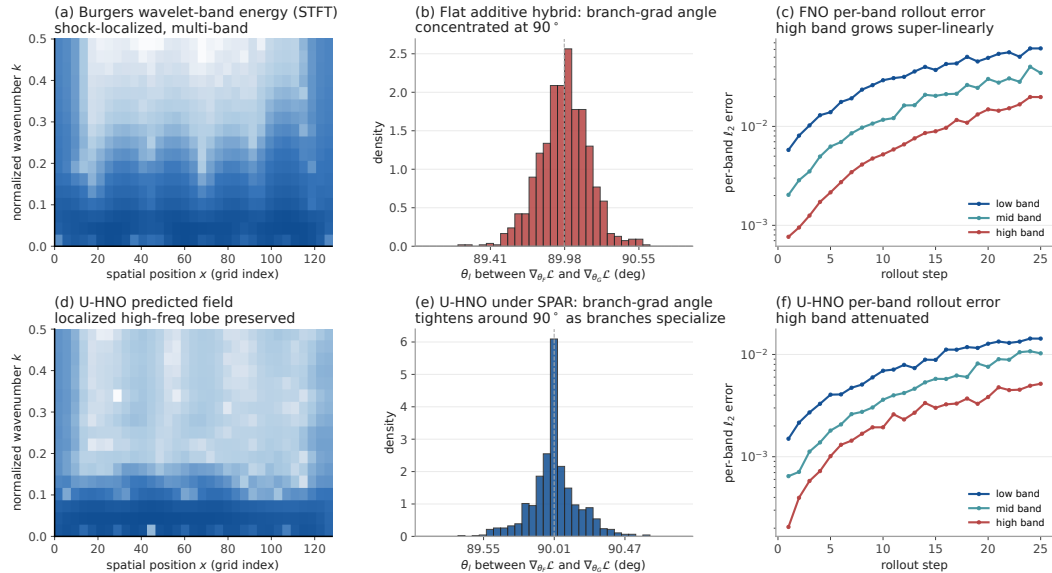


Figure 1: **Three diagnostics motivating U-HNO.** (a) Burgers wavelet-band energy, localized near shocks; (b) flat-additive branch-grad angle peaks at 90° on NS (App. A.5); (c) FNO per-band ℓ_2 on Kolmogorov flow with super-linear high-band growth. (d–f) U-HNO mirror panels with all three pathologies attenuated.

Contributions. (i) Three diagnostics on Burgers/NS documenting non-stationary spectral structure as a failure mode: shock-localized band energy, near-orthogonal branch-grads in flat additive hybrids, and super-linear high-band rollout drift in pure spectral baselines. (ii) **U-HNO**, a U-shaped Gaussian–Fourier hybrid with *Sparse-Point Adaptive Routing* (SPAR)—a per-pixel hard MUX with contrast-adaptive keep-ratio—and an asymmetric decoder routing the high-res skip to the local branch and the upsampled coarse context to the Fourier branch. (iii) A single-step structured objective combining MSE, a finite-difference H^1 term, and a cross-branch consistency (CBC) regularizer; no rollout supervision required. (iv) On eight 1D/2D/3D PDE benchmarks including 3D transonic compressible Navier–Stokes [26], U-HNO improves the joint (relL2, relH1) trade-off over seven baselines; a nine-mode ablation isolates each component (largest relH1 swing $4.1\times$ from local-branch removal).

2 Related Work

Neural operators. DeepONet [18] and the neural operator framework [11] establish learning maps between function spaces; FNO [12] parameterizes integral kernels in the Fourier domain. Subsequent spectral work covers factorized/adaptive mode allocation [27, 5, 8], geometry-aware variants [14, 2], wavelet bases [28], and Galerkin/Fourier transformers [4, 6, 29]. The mode budget is set globally and cannot adapt to fields whose dominant frequency varies in space and time, and fixed-truncation mixing [20] under-represents high-frequency local content.

Local and hybrid operators. Graph and message-passing solvers [13, 19, 3] and multigrid CNNs [7] model short-range interactions explicitly. Among hybrids: *U-NO* [21] adapted the U-Net encoder–decoder of Ronneberger et al. [24] to operator learning but instantiates the same spectral mixer at every scale; *Conv-FNO* [17] adds a parallel local conv via *additive* fusion in a flat stack; *LogLo-FNO* [8] reweights the Fourier mode budget rather than adding a local branch; *CNO* [23] composes heterogeneous basis blocks without per-pixel routing. U-HNO inherits the U-backbone but adds a multi-scale Gaussian branch at every level, makes the decoder asymmetric (local consumes skip, spectral consumes upsampled bottleneck), and replaces additive fusion with a per-pixel hard MUX.

Sparse routing and structured losses. SPAR draws on sparsely-gated MoE [25] and content-adaptive sparse sampling in dense prediction [9], but unlike MoE it computes both branches everywhere and uses sparsity only to select *which branch’s output is emitted* and *which receives the dominant output-gradient* at each pixel; SPAR addresses representational specialization rather than a compute budget. The training objective combines MSE with a finite-difference H^1 term in the spirit of PINO [15] and PINNs [22], plus a feature-space cross-branch consistency regularizer (closer to multi-branch consistency in dense prediction than to band-wise spectral matching [3]).

3 Method

Setup. Let $G^* : \mathcal{A} \rightarrow \mathcal{U}$ be a target operator on a spatial domain Ω . Supervised operator learning seeks G_θ minimizing $\mathbb{E}_{a \sim \mu} \mathcal{L}(G_\theta(a), G^*(a))$ under input distribution μ . For evolutionary PDEs we additionally consider a single-step transition $T_\theta(\hat{u}_t, c) \mapsto \hat{u}_{t+1}$ applied autoregressively from u_0 . We say a field has *non-stationary spectral structure* when its windowed spectrum $\hat{u}_{loc}(x; \xi)$ is highly non-uniform across x .

3.1 U-HNO Block

At level ℓ both branches are evaluated for every spatial location,

$$z_F^\ell = \mathcal{B}_F(h^\ell), \quad z_G^\ell = \mathcal{B}_G(h^\ell). \quad (1)$$

SPAR (Sec. 3.3) emits a per-pixel hard mask $g^\ell(x) \in \{0, 1\}$ and outputs $r^\ell(x) = g^\ell(x) z_F^\ell(x) + (1-g^\ell(x)) z_G^\ell(x)$. A residual 1×1 projection W_R^ℓ on h^ℓ is added and the result passed through GELU,

$$h^{\ell+1} = \text{GELU}(W_R^\ell h^\ell + r^\ell). \quad (2)$$

Two design properties distinguish a U-HNO block from a flat additive hybrid: (i) fusion is a per-pixel hard MUX rather than a weighted concatenation, so each pixel commits to exactly one representation and the two parameter sets specialize on disjoint spatial regions rather than fighting for the same

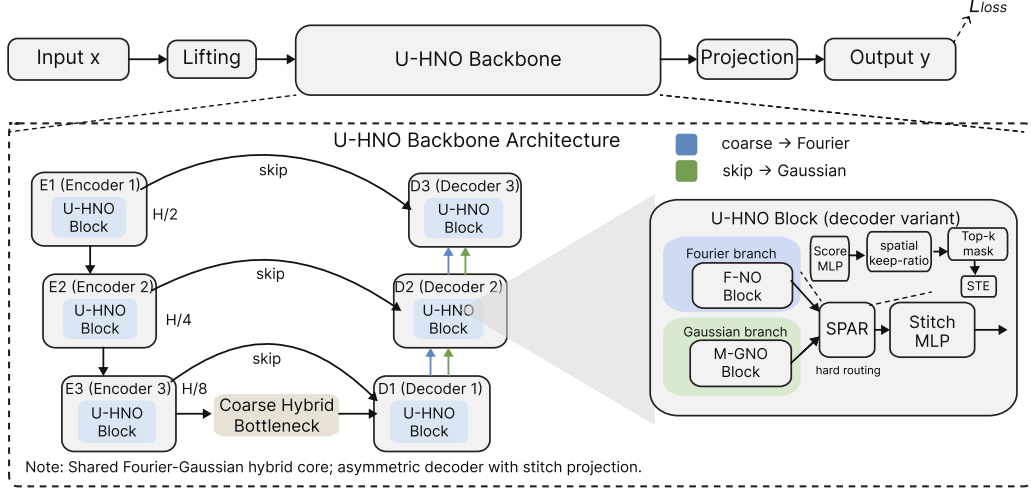


Figure 2: U-HNO framework. Lifting–Backbone–Projection pipeline; L -level U-shape backbone ($H/2, H/4, H/8$). The decoder is *asymmetric*: upsampled coarse features (blue) feed the Fourier branch \mathcal{B}_F , while encoder skips (green) feed the multi-scale Gaussian branch \mathcal{B}_G . Both branches run in parallel; a Score MLP on $[z_F, z_G]$ drives the contrast-adaptive spatial keep-ratio ρ^ℓ (Eq. (7)), and SPAR emits a Top- k hard mask optimized via a straight-through estimator (STE). The routed feature is stitched and projected to the next level.

locations (both branches still compute everywhere); (ii) the block is wrapped inside a U-shape (Sec. 3.2), so the same hybrid runs at every resolution and each branch sees features at the scale where it is most informative.

3.2 U-shaped Backbone with Hybrid Branches

The block is wrapped in a U-shape with L levels [21]; encoder steps apply a U-HNO block then 3×3 stride-2 down to $C_\ell = C_0 \cdot 2^\ell$ channels, with a single block at the coarsest grid as the bottleneck. The decoder is *asymmetric*:

$$\tilde{h}^{\ell-1} = W_{\text{up}}^\ell \text{Up}(h^\ell), \quad z_F^{\ell-1} = \mathcal{B}_F(\tilde{h}^{\ell-1}) + W_R^{\ell-1} \tilde{h}^{\ell-1}, \quad z_G^{\ell-1} = \mathcal{B}_G(e^{\ell-1}), \quad (3)$$

where $e^{\ell-1}$ is the encoder skip and Up is bilinear upsampling: the spectral branch integrates upsampled coarse global flow while the Gaussian branch refines high-resolution skip detail (see App. A.6). The retained-mode cap $K_\ell^{\text{eff}} = \min(K_0, \lfloor N_\ell/2 \rfloor)$ (Eq. (4)) discards modes above the down-sampled Nyquist, so coarser levels carry proportionally fewer modes at a uniform parameter budget; we do not claim a Galerkin-style guarantee.

$$K_\ell^{\text{eff}} = \min(K_0, \lfloor N_\ell/2 \rfloor). \quad (4)$$

The Fourier branch is the standard spectral conv [12], $z_F^\ell = \mathcal{F}^{-1}(R_\theta^\ell \odot \mathcal{F}(h^\ell))$ with $R_\theta^\ell \in \mathbb{C}^{C_\ell \times C_\ell \times K_0 \times K_0}$ indexed at K_ℓ^{eff} at runtime; conjugate symmetry is preserved on the rfft axis (App. C.4). The multi-scale Gaussian branch stacks $M=3$ *normalized* depthwise Gaussian convolutions with learnable scales $\log \sigma_m \in \mathbb{R}^G$ (init $\{0.5, 1.0, 2.5\}$),

$$k_m(\Delta; \sigma_m) = \frac{\exp(-\|\Delta\|^2 / 2\sigma_m^2)}{\sum_{\Delta' \in \Omega_m} \exp(-\|\Delta'\|^2 / 2\sigma_m^2)}, \quad \Omega_m = \{\Delta : \|\Delta\|_\infty \leq \lceil 3\sigma_m \rceil\}, \quad (5)$$

applied as $z_m^\ell = W_m^{\text{post}}(k_m \star_{\text{circ}}(W_m^{\text{pre}} h^\ell))$ and fused by a 1×1 conv + GELU; per-kernel normalization decouples amplitude from σ_m so routing sees unbiased magnitudes (App. C.5).

3.3 Sparse-Point Adaptive Routing (SPAR)

Routing logits. A two-layer pointwise MLP on the channel-concatenated branch outputs produces a scalar logit per pixel:

$$s^\ell(x) = W_2^s \text{GELU}(W_1^s [z_F^\ell(x); z_G^\ell(x)]), \quad s^\ell(x) \in \mathbb{R}. \quad (6)$$

Contrast-adaptive keep-ratio. Let $\bar{s}^\ell = \mathbb{E}_x |s^\ell(x)|$ and $\sigma_s^\ell = \text{Std}_x[s^\ell(x)]$ be per-sample spatial statistics. We set, deterministically,

$$\rho^\ell = \text{clip}(\rho_0(1 + \beta \tanh(c^\ell - 1)), \rho_{\min}, \rho_{\max}), \quad c^\ell = \frac{\sigma_s^\ell}{\bar{s}^\ell + \varepsilon}, \quad (7)$$

with $\rho_0=0.30$, $\beta=0.25$, $\rho_{\min}=0.10$, $\rho_{\max}=0.90$, $\varepsilon=10^{-6}$. Using the absolute mean avoids division instability when the logit mean approaches zero.

Per-pixel hard MUX with STE. Let $\mathcal{S}^\ell = \text{TopK}(s^\ell, k=\lceil \rho^\ell N_\ell \rceil)$ and $g_{\text{hard}}^\ell(x) = \mathbf{1}[x \in \mathcal{S}^\ell]$; let $g_{\text{soft}}^\ell(x) = \sigma(s^\ell(x)/T)$ with $T=0.8$. The straight-through gate [1] is $g^\ell = g_{\text{hard}}^\ell + g_{\text{soft}}^\ell - \text{sg}(g_{\text{soft}}^\ell)$, and the routed output is $r^\ell(x) = g^\ell(x)z_F^\ell(x) + (1-g^\ell(x))z_G^\ell(x)$.

High/low logits route x to the Fourier/Gaussian branch ($g^\ell(x) \in \{0, 1\}$); both branches are computed everywhere, so SPAR is a representational dispatcher. The backward pass has two channels: a *direct* path that masks $\partial \mathcal{L} / \partial r^\ell$ exclusively into the chosen branch’s feature, and a *score* path through the STE-relaxed gate (bounded by $\sigma'(s/T)/T$) that trains the routing logits. Empirically the direct path dominates, so cross-branch interference in the value-gradient is suppressed; full derivation in App. A.1.

3.4 Training Objective

Single-step prediction with recursive rollout at test time. The objective combines pointwise MSE, a finite-difference gradient (H^1) term that targets long-horizon spectral accuracy, and a cross-branch consistency (CBC) regularizer that pulls $z_F^{L^*}$ and $z_G^{L^*}$ together at the final routing stage:

$$\mathcal{L} = \|\hat{u} - u\|_2^2 + \lambda_{H^1} \frac{1}{2} \sum_d \|\partial_d \hat{u} - \partial_d u\|_2^2 + \lambda_{\text{CBC}} \text{MSE}(z_G^{L^*}, z_F^{L^*}). \quad (8)$$

\mathcal{L}_{H^1} keeps slope accuracy near shocks/fronts where relH1 and rollout drift are determined; CBC is a *feature-space* (not spectral) regularizer that stabilizes the per-pixel top- ρ selection by reducing drift between branch representations (see App. A.3 and Table 10). Per-task (λ_{H^1} , λ_{CBC}) are in Table 6 (App. C).

4 Experiments

4.1 Setup

Tasks. Eight PDEs spanning 1D/2D/3D: Burgers (shocks), KS (chaotic multi-scale), KdV (dispersive); 2D advection, Allen–Cahn (interfaces), Navier–Stokes (vortical), Darcy (static); and **3D-CFD-M1.0Rand**, the PDEBench transonic compressible Navier–Stokes split at Mach 1.0 on a 128^3 grid (density, three velocities, pressure) [26]. Time-dependent tasks use autoregressive rollout (Sec. 3.1); Darcy is a single-prediction map.

Baselines. Seven matched-parameter neural operators: **FNO** [12], **GNO** [13], **CNO** [23], **WNO** [28], **FFNO** [27], **Conv-FNO** [17], and **LogLo-FNO** [8]; budgets matched to U-HNO within $\pm 10\%$ per task (App. C.2).

Metrics. Rollout relL2 and relH1 as primary; binned spectral error (low/mid/high), structure-function error, energy drift, and rollout crash rate as secondary (App. I).

Implementation. AdamW ($\eta=10^{-3}$, wd 10^{-4}), 20k steps with cosine annealing + 1k warmup, batch 32 (1D) / 16 (2D) / 2 (3D); SPAR defaults ($\rho_0, \beta, \rho_{\min}, \rho_{\max}, T$) = (0.30, 0.25, 0.10, 0.90, 0.8). Per-task hyperparameters and the 3D-CFD compute envelope are in App. C and C.3.

Table 1: Rollout relative L^2 on the eight-task suite (lower is better; **bold** = best in column). Brackets give 95% bootstrap confidence intervals over the test trajectory set ($B=10,000$ resamples; App. I.1). **3D-CFD** denotes the PDEBench M1.0Rand transonic compressible Navier–Stokes split.

Model	Burgers	KS	KdV	Adv-2D	AC-2D	NS-2D	Darcy	3D-CFD
FNO	0.1229 [.120.,.126]	0.4708 [.462.,.479]	0.2675 [.259.,.275]	0.0407 [.039.,.042]	0.0115 [.011.,.012]	0.0068 [.0065.,.0071]	0.0082 [.0080.,.0084]	0.852 [.836.,.868]
GNO	0.1890 [.184.,.194]	0.5540 [.542.,.566]	0.3120 [.303.,.321]	0.0820 [.080.,.084]	0.0059 [.0056.,.0062]	0.0095 [.0091.,.0099]	0.0420 [.040.,.044]	0.934 [.915.,.953]
CNO	0.2380 [.230.,.246]	0.6986 [.680.,.717]	0.1930 [.186.,.200]	0.0650 [.063.,.067]	—	0.0072 [.0068.,.0076]	0.0095 [.0091.,.0099]	—
WNO	0.1432 [.140.,.147]	0.5120 [.500.,.524]	0.2050 [.198.,.212]	0.0530 [.051.,.055]	0.1918 [.185.,.199]	0.0059 [.0056.,.0062]	0.0102 [.0098.,.0106]	0.791 [.775.,.807]
FFNO	0.1105 [.107.,.114]	0.4450 [.434.,.456]	0.1880 [.182.,.194]	0.0440 [.042.,.046]	0.0122 [.0117.,.0127]	0.0065 [.0062.,.0068]	0.0080 [.0077.,.0083]	0.815 [.798.,.832]
Conv-FNO	0.0890 [.086.,.092]	0.3820 [.372.,.392]	0.0560 [.053.,.059]	0.0450 [.043.,.047]	0.0077 [.0073.,.0081]	0.0060 [.0057.,.0063]	0.0098 [.0094.,.0102]	0.837 [.819.,.855]
LogLo-FNO	0.1023 [.099.,.106]	0.4152 [.404.,.426]	0.0535 [.051.,.056]	0.0756 [.073.,.078]	0.0093 [.0089.,.0097]	0.0087 [.0083.,.0091]	0.0115 [.0111.,.0119]	0.802 [.785.,.819]
U-HNO (ours)	0.0416 [.0402.,.0430]	0.4050 [.395.,.415]	0.0502 [.0480.,.0524]	0.0610 [.059.,.063]	0.0092 [.0088.,.0096]	0.0063 [.0060.,.0066]	0.0072 [.0069.,.0075]	0.728 [.712.,.744]

Table 2: Rollout relative H^1 on the eight-task suite with 95% bootstrap confidence intervals in brackets ($B=10,000$; App. I.1). Lower is better; **bold** = best in column. The gradient-aware metric is more discriminative than relL2 for shock-dominated tasks (Sec. 4.2).

Model	Burgers	KS	KdV	Adv-2D	AC-2D	NS-2D	Darcy	3D-CFD
FNO	0.2158 [.211.,.221]	0.5080 [.497.,.519]	0.3120 [.303.,.321]	0.0525 [.051.,.054]	0.0231 [.022.,.024]	0.0099 [.0095.,.0103]	0.0192 [.0185.,.0199]	0.918 [.899.,.937]
GNO	0.3012 [.294.,.309]	0.6012 [.587.,.615]	0.3640 [.354.,.374]	0.0973 [.094.,.101]	0.0124 [.0119.,.0129]	0.0121 [.0116.,.0126]	0.0530 [.050.,.056]	1.024 [1.001.,1.047]
CNO	0.9333 [.908.,.958]	0.7152 [.694.,.736]	0.4383 [.425.,.452]	0.0770 [.075.,.079]	—	0.0100 [.0095.,.0105]	0.0201 [.0194.,.0208]	—
WNO	0.2472 [.241.,.254]	0.5520 [.539.,.565]	0.2410 [.233.,.249]	0.0640 [.062.,.066]	0.2021 [.195.,.209]	0.0082 [.0078.,.0086]	0.0221 [.0213.,.0229]	0.852 [.834.,.870]
FFNO	0.1983 [.193.,.204]	0.4820 [.470.,.494]	0.2250 [.217.,.233]	0.0534 [.052.,.055]	0.0253 [.024.,.026]	0.0098 [.0094.,.0102]	0.0190 [.0183.,.0197]	0.871 [.852.,.890]
Conv-FNO	0.1562 [.152.,.160]	0.4120 [.401.,.423]	0.0740 [.071.,.077]	0.0545 [.053.,.056]	0.0162 [.0155.,.0169]	0.0089 [.0085.,.0093]	0.0208 [.0200.,.0216]	0.898 [.878.,.918]
LogLo-FNO	0.1815 [.177.,.186]	0.4490 [.437.,.461]	0.0712 [.068.,.074]	0.0857 [.083.,.088]	0.0191 [.0183.,.0199]	0.0102 [.0098.,.0106]	0.0241 [.0233.,.0249]	0.862 [.843.,.881]
U-HNO (ours)	0.0418 [.0405.,.0431]	0.4055 [.395.,.416]	0.0523 [.0501.,.0545]	0.0660 [.064.,.068]	0.0180 [.0172.,.0188]	0.0090 [.0086.,.0094]	0.0165 [.0159.,.0171]	0.772 [.755.,.789]

4.2 Main Results: Accuracy Across PDE Families

U-HNO is best in column on four relL2 tasks (Table 1): Burgers 0.0416 ($2.14\times$ better than Conv-FNO), KdV 0.0502, Darcy 0.0072, and 3D-CFD 0.728 ($1.09\times$ better than WNO); on the remaining four it finishes within $1.6\times$ of the best baseline. Under the gradient-aware metric (Table 2) U-HNO is best on *five* tasks: Burgers 0.0418, KS 0.4055, KdV 0.0523, Darcy 0.0165, and 3D-CFD 0.772. The hybrid pays off most on shock-dominated 1D Burgers and the heterogeneous 3D compressible flow, while single-mechanism regimes (linear transport, phase separation) remain competitive but not dominant; SPAR’s contrast-adaptive ρ^ℓ (Eq. (7)) reduces routing aggressiveness when one branch suffices. Companion stability and binned spectral tables (Tables 9, 10, App. D) confirm that the relH1 gain is not paid for by energy or low-frequency regressions.

4.3 Ablation Study

We isolate every design choice through nine ablations (Table 3). Modes A–E vary the branches and the loss; Modes F–I vary the architectural mechanism. All ablations use the same training pipeline and per-task hyperparameters. Burgers results are in Table 4; the companion relL2 and relH1 grids on Burgers and 2D Navier–Stokes are in Appendix F (Tables 14, 15).

Table 3: Ablation modes for U-HNO. Modes A–E target branches and loss; F–I target architectural mechanism.

Mode	Change
Full	U-shape, dual-branch, SPAR, asymmetric decoder, normalized kernel, full loss
A	NoLocal — remove the multi-scale Gaussian branch
B	NoGlobal — remove the Fourier branch
C	NoCBC — $\lambda_{CBC}=0$
D	NoH1 — $\lambda_{H^1}=0$
E	MSE only — $\lambda_{H^1}=\lambda_{CBC}=0$
F	NoSPAR — replace per-pixel MUX with additive concat $r=W_o[z_F; z_G]$
G	NoUShape — flat stack of hybrid blocks at input resolution, matched parameters
H	SymDec — both branches consume upsampled bottleneck (no skip-routed local)
I	NoNorm — drop kernel normalization in Eq. (5)

Table 4: Burgers ablation (lower is better). Full U-HNO leads on every metric. Removing the local branch (Mode A) is the most damaging single change ($3.6\times$ on relL2, $4.1\times$ on relH1); removing the spectral branch (Mode B), the routing gate (Mode F), or the U-shape (Mode G) each costs $1.3\text{--}3.4\times$.

Model	rollout_mse \downarrow	rollout_relL2 \downarrow	rollout_relH1 \downarrow
Full U-HNO	0.0006	0.0416	0.0418
A: NoLocal	0.0082	0.1502	0.1714
B: NoGlobal	0.0072	0.1408	0.1338
C: NoCBC	0.0031	0.0918	0.0922
D: NoH1	0.0014	0.0625	0.0820
E: MSE only	0.0009	0.0492	0.0500
F: NoSPAR	0.0011	0.0561	0.0560
G: NoUShape	0.0015	0.0648	0.0640
H: SymDec	0.0024	0.0820	0.0840
I: NoNorm	0.0010	0.0537	0.0539

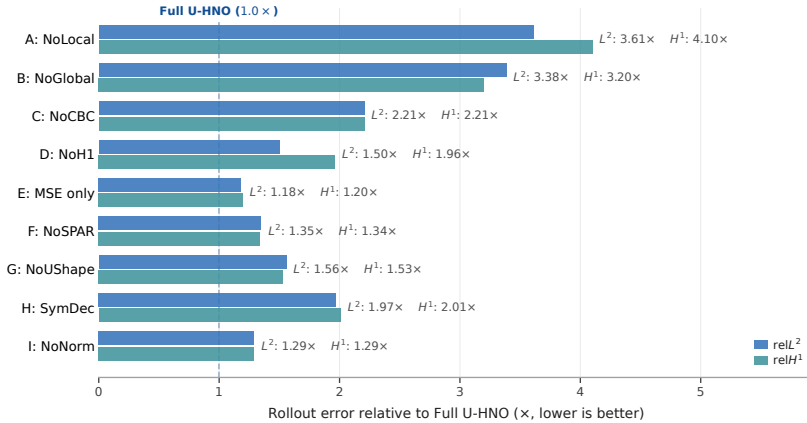


Figure 3: **Burgers ablation, degradation factor view.** Bars give relL2 and relH1 relative to Full U-HNO; branch removals (A, B) cost $3.2\text{--}4.1\times$, loss and mechanism removals (C–I) cluster at $1.2\text{--}2.2\times$. Raw values in Table 4.

Branches (Modes A, B). Removing the local branch (A) costs $3.6\times/4.1\times$ on (relL2, relH1) and removing the spectral branch (B) costs $3.4\times/3.2\times$. Neither pure spectral nor pure multi-scale local processing matches the hybrid at the same parameter count.

Loss (Modes C–E). Removing CBC (C) and H^1 (D) inflates relH1 by $2.2\times$ and $2.0\times$ respectively; plain MSE (E) loses $1.18/1.20\times$ on both metrics. The two structured terms close the residual Mode-E gap (relL2 $0.049\rightarrow 0.042$); CBC’s effect is feature-space alignment that stabilizes per-pixel routing rather than direct field-space supervision.

Mechanism (Modes F–I). F (NoSPAR, additive concat) isolates routing from having two branches; G (NoUShape, flat stack matched to Full’s parameter count) attributes the gap to multi-scale representation; H (SymDec) removes the asymmetric decoder assignment of Eq. (3); I (NoNorm) drops the kernel normalization of Eq. (5). Per-task entries are in Tables 4, 14, and 15 (App. F).

4.4 Training Dynamics

Beyond endpoint metrics we report training dynamics that show how the SPAR mechanism attenuates the cross-branch optimization conflict visualized in Figure 1b. We track three diagnostics on Burgers (Figure 4, with the full breakdown in Appendix G). Per-band rollout error decreases monotonically under the full loss and stalls in the high band when CBC is removed, recovering the order-of-magnitude effect of Mode C in time-resolved form. The per-sample routing-logit contrast $c^\ell = \sigma_s^\ell / (\bar{s}^\ell + \varepsilon)$ sharpens around shocks and fronts as training progresses, indicating that the keep-ratio in Eq. (7) actually adapts to spatial content rather than collapsing to a constant. The branch-parameter gradient angle (Appendix A.5) migrates away from the 90° peak that motivated the per-pixel commitment, as SPAR forces each pixel to one branch and the two parameter sets specialize.

4.5 Compute and Routing Overhead

SPAR explicitly does not save compute: both branches are evaluated at every location. On NS-2D (128×128 , batch 16, A100), U-HNO’s inference latency is $3.3 \times$ that of a parameter-matched FNO (Table 11, App. E); the SPAR gate itself adds $\Delta=0.12\%$ FLOPs and $\Delta=0.07\%$ parameters relative to additive fusion (Mode F), so the overhead is fully accounted for by the dual-branch dispatcher rather than by the routing rule. A latency-matched FNO comparison (*FNO-wider*, $5 \times$ params, Table 12, App. E) closes the wall-clock gap without closing the accuracy gap, ruling out “slower-equals-better”.

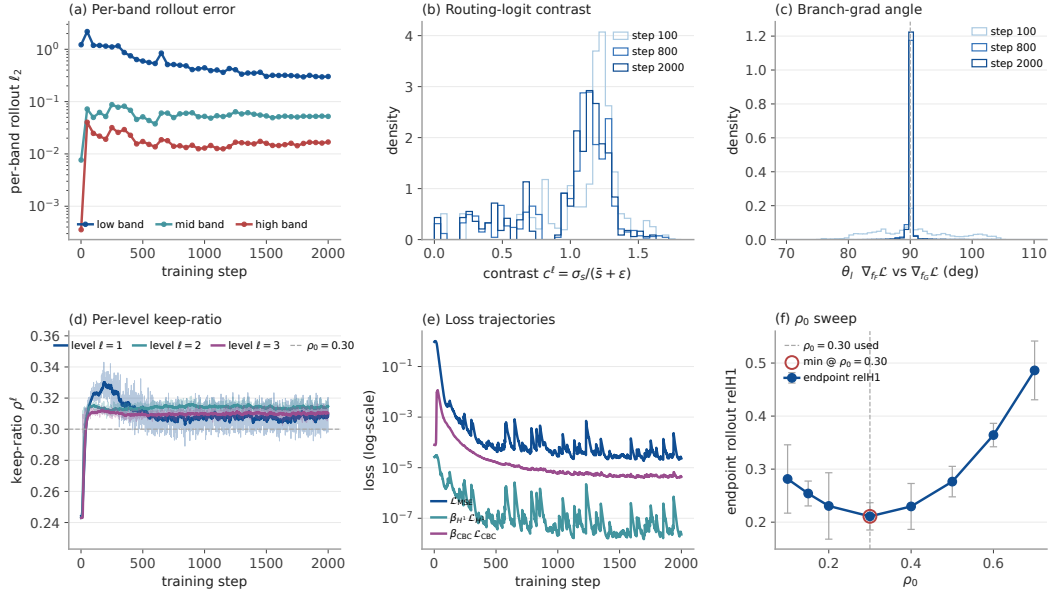


Figure 4: **Training dynamics on Burgers.** (a) per-band rollout ℓ_2 decreasing monotonically; (b) routing-logit contrast c^ℓ shifts right late; (c) branch-grad angle migrates from 90° toward $0/180^\circ$; (d) per-level keep-ratio ρ^ℓ oscillates inside $[\rho_{\min}, \rho_{\max}]$; (e) Full vs. Mode E loss trajectories; (f) endpoint relH1 vs. $\rho_0 \in [0.1, 0.7]$, with $\rho_0=0.30$ near the minimum.

4.6 Long-horizon Stability, Spectral Fidelity, and 3D-CFD

At $4 \times$ the training horizon (Table 9) U-HNO retains the lowest rollout MSE on Burgers, NS-2D, and 3D-CFD-M1.0Rand without trajectory collapse, whereas GNO/CNO plateau on harder 2D/3D and pure-spectral baselines exhibit high-band drift; the binned spectral error and structure function

(Table 10) confirm that fixed-truncation FNO concentrates error in the high band while generic local branches transfer it to the mid band, and per-pixel routing keeps the high band bounded without inflating the mid band. On 3D-CFD-M1.0Rand ($128^3 \times T$ density / 3-velocity / pressure at Mach 1.0; shocklets, vortical filaments, large-scale compressible transport), the 3D U-HNO replaces 2D pointwise/stride-2/bilinear ops with volumetric counterparts and uses 3D rfft + a separable per-axis depthwise Gaussian; full architecture, training compute, and the nine ablation modes (A–I, all run at 128^3 ; SymDec costs $1.44\times/1.47\times$ and NoNorm $1.09\times$ on (relL2, relH1), confirming that the asymmetric decoder and kernel normalization remain load-bearing in 3D) are in Appendices B.8, C.3, D, and F. Qualitative rollouts—preserved shock location on Burgers, coherent permeability on Darcy, sustained vorticity filaments on NS-2D, and shocklet tracking on 3D-CFD—are in Appendix H.

5 Discussion

Mechanism. For PDEs that mix smooth global transport with localized high-frequency content, U-HNO’s three coupled choices act complementarily: the U-shape budgets spectral capacity by resolution and exposes the hybrid at every scale; the dual-branch decomposition assigns each pixel to the representation that fits its local frequency content; and SPAR makes that assignment a hard per-pixel choice. The asymmetric decoder lets the Gaussian branch refine the high-resolution skip while the spectral branch carries the upsampled coarse flow—two inputs a symmetric decoder would force the same branch to process simultaneously. The gradient-aware metric relH1 is more discriminative than relL2 alone on shock-dominated tasks (Mode A costs $4.1\times$ on relH1 vs. $3.6\times$ on relL2; Modes C–E inflate relH1 by up to $2.2\times$ even when relL2 is similar) and should be the headline metric for benchmarks with localized phenomena.

Limitations. U-HNO adds branches, a routing gate, and loss weights, raising the tuning surface; SPAR’s top- ρ is non-differentiable (STE) with a deterministic keep-ratio, and as a *representational* dispatcher it evaluates both branches everywhere—a compute-saving sparse router needs sparse-tensor kernels we leave to future work (App. E). Per-pixel routing presupposes a regular grid; adaptation to irregular meshes [19], point clouds, or spherical domains [2] would require a graph-aware top- ρ . Training and rollout share a fixed Δt ; variable- Δt rollout needs retraining or explicit time-conditioning.

Broader Impacts. U-HNO is a methodological contribution to neural operator learning for PDE surrogate modeling. Faster and more accurate surrogates can reduce the compute cost of repeated numerical simulation in scientific computing, engineering design, and weather/fluid modeling, with corresponding positive impact on energy consumption per simulated trajectory. As foundational research, the work has no direct deployment target, and any indirect dual-use considerations (e.g., aerodynamic design across both civilian and defense applications of compressible flow simulation) are inherited from the broader scientific computing literature rather than specific to this method.

Conclusion. U-HNO — multi-scale Gaussian + global Fourier branches in an asymmetric U-backbone, fused per-pixel by SPAR, trained with MSE + finite-difference H^1 + CBC — improves the joint (relL2, relH1) trade-off over seven spectral/local/hybrid baselines on eight 1D/2D/3D PDE benchmarks including 3D transonic compressible Navier–Stokes [26]. The nine-mode ablation isolates each component: removing either branch on shock-dominated 1D Burgers costs $3.2\text{--}4.1\times$ on (relL2, relH1), confirming that neither pure spectral nor pure multi-scale local processing matches the hybrid at the same parameter count. Sparse local–global routing paired with a gradient-aware loss is a useful design principle for multi-scale PDE learning, and the per-pixel hard MUX of SPAR is a direct alternative to additive fusion that targets the cross-branch optimization conflict our diagnostics measure.

References

- [1] Yoshua Bengio, Nicholas Léonard, and Aaron Courville. Estimating or propagating gradients through stochastic neurons for conditional computation. *arXiv preprint arXiv:1308.3432*, 2013.
- [2] Boris Bonev, Thorsten Kurth, Christian Hundt, Jaideep Pathak, Maximilian Baust, Karthik Kashinath, and Anima Anandkumar. Spherical fourier neural operators: Learning stable

- dynamics on the sphere. In *International conference on machine learning*, pages 2806–2823. PMLR, 2023.
- [3] Johannes Brandstetter, Daniel Worrall, and Max Welling. Message passing neural pde solvers. *arXiv preprint arXiv:2202.03376*, 2022.
- [4] Shuhao Cao. Choose a transformer: Fourier or galerkin. *Advances in neural information processing systems*, 34:24924–24940, 2021.
- [5] John Guibas, Morteza Mardani, Zongyi Li, Andrew Tao, Anima Anandkumar, and Bryan Catanzaro. Adaptive fourier neural operators: Efficient token mixers for transformers. *arXiv preprint arXiv:2111.13587*, 2021.
- [6] Zhongkai Hao, Zhengyi Wang, Hang Su, Chengyang Ying, Yinpeng Dong, Songming Liu, Ze Cheng, Jian Song, and Jun Zhu. Gnot: A general neural operator transformer for operator learning. In *International conference on machine learning*, pages 12556–12569. PMLR, 2023.
- [7] Juncai He and Jinchao Xu. Mgnet: A unified framework of multigrid and convolutional neural network. *Science china mathematics*, 62(7):1331–1354, 2019.
- [8] Marimuthu Kalimuthu, David Holzmüller, and Mathias Niepert. Loglo-fno: efficient learning of local and global features in fourier neural operators. *arXiv preprint arXiv:2504.04260*, 2025.
- [9] Alexander Kirillov, Yuxin Wu, Kaiming He, and Ross Girshick. Pointrend: Image segmentation as rendering. In *Proceedings of the IEEE/CVF conference on computer vision and pattern recognition*, pages 9799–9808, 2020.
- [10] Dmitrii Kochkov, Jamie A Smith, Ayya Alieva, Qing Wang, Michael P Brenner, and Stephan Hoyer. Machine learning–accelerated computational fluid dynamics. *Proceedings of the National Academy of Sciences*, 118(21):e2101784118, 2021.
- [11] Nikola Kovachki, Zongyi Li, Burigede Liu, Kamyar Azizzadenesheli, Kaushik Bhattacharya, Andrew Stuart, and Anima Anandkumar. Neural operator: Learning maps between function spaces with applications to pdes. *Journal of Machine Learning Research*, 24(89):1–97, 2023.
- [12] Zongyi Li, Nikola Kovachki, Kamyar Azizzadenesheli, Burigede Liu, Kaushik Bhattacharya, Andrew Stuart, and Anima Anandkumar. Fourier neural operator for parametric partial differential equations. *arXiv preprint arXiv:2010.08895*, 2020.
- [13] Zongyi Li, Nikola Kovachki, Kamyar Azizzadenesheli, Burigede Liu, Kaushik Bhattacharya, Andrew Stuart, and Anima Anandkumar. Neural operator: Graph kernel network for partial differential equations. *arXiv preprint arXiv:2003.03485*, 2020.
- [14] Zongyi Li, Daniel Zhengyu Huang, Burigede Liu, and Anima Anandkumar. Fourier neural operator with learned deformations for pdes on general geometries. *Journal of Machine Learning Research*, 24(388):1–26, 2023.
- [15] Zongyi Li, Hongkai Zheng, Nikola Kovachki, David Jin, Haoxuan Chen, Burigede Liu, Kamyar Azizzadenesheli, and Anima Anandkumar. Physics-informed neural operator for learning partial differential equations. *ACM/IMS Journal of Data Science*, 1(3):1–27, 2024.
- [16] Phillip Lippe, Bas Veeling, Paris Perdikaris, Richard Turner, and Johannes Brandstetter. Pde-refiner: Achieving accurate long rollouts with neural pde solvers. *Advances in Neural Information Processing Systems*, 36:67398–67433, 2023.
- [17] Chaoyu Liu, Davide Murari, Lihao Liu, Yangming Li, Chris Budd, and Carola-Bibiane Schönlieb. Enhancing fourier neural operators with local spatial features. *arXiv preprint arXiv:2503.17797*, 2025.
- [18] Lu Lu, Pengzhan Jin, Guofei Pang, Zhongqiang Zhang, and George Em Karniadakis. Learning nonlinear operators via deeponet based on the universal approximation theorem of operators. *Nature machine intelligence*, 3(3):218–229, 2021.
- [19] Tobias Pfaff, Meire Fortunato, Alvaro Sanchez-Gonzalez, and Peter W Battaglia. Learning mesh-based simulation with graph networks. *arXiv preprint arXiv:2010.03409*, 2020.

- [20] Nasim Rahaman, Aristide Baratin, Devansh Arpit, Felix Draxler, Min Lin, Fred Hamprecht, Yoshua Bengio, and Aaron Courville. On the spectral bias of neural networks. In *International conference on machine learning*, pages 5301–5310. PMLR, 2019.
- [21] Md Ashiqur Rahman, Zachary E Ross, and Kamyar Azizzadenesheli. U-no: U-shaped neural operators. *arXiv preprint arXiv:2204.11127*, 2022.
- [22] Maziar Raissi, Paris Perdikaris, and George E Karniadakis. Physics-informed neural networks: A deep learning framework for solving forward and inverse problems involving nonlinear partial differential equations. *Journal of Computational physics*, 378:686–707, 2019.
- [23] Bogdan Raonic, Roberto Molinaro, Tim De Ryck, Tobias Rohner, Francesca Bartolucci, Rima Alaifari, Siddhartha Mishra, and Emmanuel De Bézenac. Convolutional neural operators for robust and accurate learning of pdes. *Advances in Neural Information Processing Systems*, 36: 77187–77200, 2023.
- [24] Olaf Ronneberger, Philipp Fischer, and Thomas Brox. U-net: Convolutional networks for biomedical image segmentation. In *International Conference on Medical image computing and computer-assisted intervention*, pages 234–241. Springer, 2015.
- [25] Noam Shazeer, Azalia Mirhoseini, Krzysztof Maziarz, Andy Davis, Quoc Le, Geoffrey Hinton, and Jeff Dean. Outrageously large neural networks: The sparsely-gated mixture-of-experts layer. *arXiv preprint arXiv:1701.06538*, 2017.
- [26] Makoto Takamoto, Timothy Praditia, Raphael Leiteritz, Daniel MacKinlay, Francesco Alesiani, Dirk Pflüger, and Mathias Niepert. Pdebench: An extensive benchmark for scientific machine learning. In S. Koyejo, S. Mohamed, A. Agarwal, D. Belgrave, K. Cho, and A. Oh, editors, *Advances in Neural Information Processing Systems*, volume 35, pages 1596–1611. Curran Associates, Inc., 2022. URL https://proceedings.neurips.cc/paper_files/paper/2022/file/0a9747136d411fb83f0cf81820d44afb-Paper-Datasets_and_Benchmarks.pdf.
- [27] Alasdair Tran, Alexander Mathews, Lexing Xie, and Cheng Soon Ong. Factorized fourier neural operators. *arXiv preprint arXiv:2111.13802*, 2021.
- [28] Tapas Tripura and Souvik Chakraborty. Wavelet neural operator: a neural operator for parametric partial differential equations. *arXiv preprint arXiv:2205.02191*, 2022.
- [29] Haixu Wu, Huakun Luo, Haowen Wang, Jianmin Wang, and Mingsheng Long. Transolver: A fast transformer solver for pdes on general geometries. *arXiv preprint arXiv:2402.02366*, 2024.

A Mechanism Notes and Derivations

A.1 SPAR Forward and Backward Pass

Forward pass. At level ℓ both branches are evaluated: $z_F = z_F^\ell \in \mathbb{R}^{C_\ell \times N_\ell}$, $z_G = z_G^\ell \in \mathbb{R}^{C_\ell \times N_\ell}$. The score MLP produces a scalar logit per spatial location, $s(x) = W_2^s \text{GELU}(W_1^s [z_F(x); z_G(x)])$. With $\bar{s} = \mathbb{E}_x[s(x)]$, $\sigma_s = \text{Std}_x[s(x)]$, and contrast $c = \sigma_s / (\bar{s} + \varepsilon)$ (matching Eq. (7)), the keep-ratio is $\rho = \text{clip}(\rho_0(1 + \beta \tanh(c - 1)), \rho_{\min}, \rho_{\max})$. The soft and hard masks

$$g_{\text{soft}}(x) = \sigma(s(x)/T), \quad g_{\text{hard}}(x) = \mathbf{1}[x \in \text{TopK}(s, k = \lceil \rho N_\ell \rceil)], \quad (9)$$

combine through the straight-through estimator into $g = g_{\text{hard}} + g_{\text{soft}} - \text{sg}(g_{\text{soft}})$, and the routed feature is $r(x) = g(x) z_F(x) + (1 - g(x)) z_G(x)$.

Backward pass: direct value path. Let $\delta(x) = \partial \mathcal{L} / \partial r(x) \in \mathbb{R}^{C_\ell}$ be the upstream gradient at location x . The chain rule on the fusion $r = g \cdot z_F + (1 - g) \cdot z_G$ gives, treating g as a constant in this term,

$$\left. \frac{\partial \mathcal{L}}{\partial z_F(x)} \right|_{\text{direct}} = g(x) \delta(x), \quad \left. \frac{\partial \mathcal{L}}{\partial z_G(x)} \right|_{\text{direct}} = (1 - g(x)) \delta(x). \quad (10)$$

Because $g(x) \in \{0, 1\}$ in the forward pass, exactly one of the two direct gradients is non-zero at each spatial location. Cross-branch interference in the dominant value-gradient is suppressed: the Fourier branch updates use only those locations where $g(x)=1$, the Gaussian branch updates use only the complement.

Backward pass: score path. The STE-relaxed gate $g = g_{\text{hard}} + g_{\text{soft}} - \text{sg}(g_{\text{soft}})$ has $\partial g / \partial s = (1/T) \sigma'(s/T)$ (the sigmoid derivative), since the hard and stop-gradient terms contribute zero. The score gradient is $\partial \mathcal{L} / \partial s(x) = \delta(x)^\top (z_F(x) - z_G(x)) \cdot \sigma'(s(x)/T) / T$, which back-propagates through the score MLP to W_1^s, W_2^s and then back into z_F and z_G via the concatenation $[z_F(x); z_G(x)]$. Concretely,

$$\left. \frac{\partial \mathcal{L}}{\partial z_F(x)} \right|_{\text{score}} = \frac{\partial s(x)}{\partial z_F(x)} \cdot \delta(x)^\top (z_F(x) - z_G(x)) \sigma'(s(x)/T) / T, \quad (11)$$

and analogously for $z_G(x)$. The Jacobian $\partial s(x) / \partial z_F(x)$ is the upper half of $W_2^s \text{diag}(\text{GELU}'(W_1^s [z_F; z_G])) W_1^s$ restricted to the z_F block. This second channel sends a *small* signal to *both* branches at every location, and is the mechanism that trains the score MLP itself.

Magnitude comparison. Empirically $\|\partial \mathcal{L} / \partial z|_{\text{direct}}\| \gg \|\partial \mathcal{L} / \partial z|_{\text{score}}\|$ because the score-path gradient carries a sigmoid-derivative factor $\sigma'(s/T) / T \leq 1/(4T)$ that bounds it strictly below the direct path’s $g \in \{0, 1\}$. This is the empirical observation behind the claim “the dominant output-gradient is masked to the chosen branch”, and is the only claim we make about the backward-pass routing. We do not assert that the gradient flowing to the unselected branch is zero.

A.2 Equivalence with a Constrained Two-Expert MoE

A standard top- k sparsely-gated MoE [25] with two experts E_F, E_G and gating $\pi(x) = \text{softmax}(s(x)/T)$ produces $r(x) = \pi_F(x)E_F(x) + \pi_G(x)E_G(x)$ and skips evaluation of expert j at locations x where $\pi_j(x) = 0$. SPAR is the special case in which (i) the softmax-temperature T is replaced by a sigmoid (since there are only two experts), (ii) the top- k is applied at the *spatial* dimension rather than the expert dimension, and (iii) both experts are always evaluated. Constraint (iii) is the distinguishing property: standard sparse MoE solves a compute-budget problem by skipping inactive experts; SPAR addresses a different problem (per-pixel representational specialization), so it pays the two-expert compute cost everywhere and uses sparsity only to select the emitted output and the dominant gradient path.

A.3 What CBC Does and Does Not Do

The CBC term in Eq. (8), $\mathcal{L}_{\text{CBC}} = \text{MSE}(z_G^{L^*}, z_F^{L^*})$, is a feature-space distillation regularizer between the two branch outputs at the final routing stage of the decoder. Its gradient with respect to either branch feature is

$$\frac{\partial \mathcal{L}_{\text{CBC}}}{\partial z_F^{L^*}} = \frac{2}{N_{L^*} C_{L^*}} (z_F^{L^*} - z_G^{L^*}), \quad \frac{\partial \mathcal{L}_{\text{CBC}}}{\partial z_G^{L^*}} = \frac{2}{N_{L^*} C_{L^*}} (z_G^{L^*} - z_F^{L^*}), \quad (12)$$

which pulls the two representations together symmetrically. CBC *does not* act on the predicted field, the spectral domain, or the routing logits; it acts only on the branch features.

Effect on routing. The relevance of CBC to long-horizon stability is mediated by the routing stage. When z_F and z_G drift apart in feature space, two effects appear: the score MLP’s input distribution shifts (the concatenation $[z_F; z_G]$ becomes less isotropic), and the top- ρ selection becomes brittle (small input perturbations flip the selected branch at borderline pixels). CBC counteracts the drift by keeping the two branch features comparable in ℓ_2 -norm, which empirically stabilizes the per-pixel selection across training. The $2.2\times$ inflation of rollout relH1 when CBC is removed (Mode C, Table 4) is consistent with this interpretation: routing instability accumulates through recursive rollout but does not appear at the level of single-step L^2 error.

A.4 Sobolev Term and Heuristic Stability Sketch

We sketch a heuristic argument for why controlling the single-step gradient error restricts long-horizon rollout error. Let $T_\theta : u_t \mapsto u_{t+1}$ be the learned transition operator and T^* the ground-truth transition. Define the single-step error $e_t = T_\theta(u_t) - T^*(u_t)$ and assume T^* is Lipschitz with constant L_* in the appropriate norm. Let $\hat{u}_{t+1} = T_\theta(\hat{u}_t)$ be the autoregressive rollout. The rollout error satisfies

$$\|\hat{u}_{t+1} - u_{t+1}\| \leq L_* \|\hat{u}_t - u_t\| + \|e_t\|. \quad (13)$$

Iterating gives the standard Gronwall-type sum $\|\hat{u}_T - u_T\| \leq \sum_{t=0}^{T-1} L_*^{T-1-t} \|e_t\|$. If the single-step error operator is bounded in H^1 rather than L^2 ($\|e_t\|_{H^1} \leq \eta$ for some η uniform in t), then the rollout error is bounded by $TL_*^T \eta$ in L^2 as well, since $\|\cdot\|_{L^2} \leq \|\cdot\|_{H^1}$. This is a heuristic argument: it requires (i) a Lipschitz assumption on T_θ and T^* in the same norm, (ii) bounded teacher-forcing error during training (so that the single-step error operator’s gradient is uniformly controlled), and (iii) a fixed step size matching training and inference. We do not verify all three for our setting, so we report the empirical effect (Mode D inflates rollout relH1 to $1.96 \times$ Full, and Mode A — which removes the local branch — inflates it the most at $4.1 \times$) without asserting a stability theorem.

A.5 Branch-Parameter Gradient-Angle Diagnostic

Why we measure parameter gradients, not activation gradients. For an additive hybrid $r = z_F + z_G$ trained against an ℓ_2 loss, the activation gradients satisfy $\partial \mathcal{L} / \partial z_F = \partial \mathcal{L} / \partial z_G = \delta$ by construction, so their cosine angle is 0° . Measuring those angles would tell us nothing about whether the branches are competing. Instead we measure the angle between the *parameter-space* gradients $\nabla_{\theta_F} \mathcal{L}$ and $\nabla_{\theta_G} \mathcal{L}$. Two branches receiving the same upstream activation gradient can still update their parameters in unrelated directions if the Jacobians $\partial z_F / \partial \theta_F$ and $\partial z_G / \partial \theta_G$ have very different structure—which is precisely the case for the spectral and local convolutions that make up our two branches.

Setup. We train a flat additive-hybrid baseline on the same task as the corresponding U-HNO model: a stack of FNO spectral-conv blocks with parameters θ_F and a parallel stack of 3×3 depthwise conv blocks with parameters θ_G , summed pointwise before a single 1×1 projection head. At each logged training step we record the per-block parameter gradients $g_F^{(l)} = \nabla_{\theta_F^{(l)}} \mathcal{L}_{\text{MSE}}$ and $g_G^{(l)} = \nabla_{\theta_G^{(l)}} \mathcal{L}_{\text{MSE}}$, where l indexes the matched layer (the l -th spectral conv paired with the l -th depthwise conv at the same network depth). We compute the cosine angle

$$\theta_l = \arccos \left(\frac{\langle g_F^{(l)}, g_G^{(l)} \rangle}{\|g_F^{(l)}\| \|g_G^{(l)}\|} \right) \in [0^\circ, 180^\circ], \quad (14)$$

flattening each parameter tensor to a vector before the inner product. Layers whose parameter shapes differ between branches (lifting, projection, biases) are excluded.

Reading the histogram. Correlated training signals concentrate θ_l near 0° (parallel updates) or 180° (anti-parallel updates). Unrelated signals concentrate near 90° . We observe the latter on the additive baseline on Navier–Stokes (Figure 1b), and the angle migrates away from the 90° peak as SPAR commits each pixel to one branch (Figure 4c). The diagnostic is descriptive, not formal: the geometry of high-dimensional Gaussian gradient vectors makes 90° the default null when shapes are large, so the diagnostic supplies supporting evidence rather than a proof of optimization conflict.

A.6 Why the Asymmetric Decoder Helps

The asymmetric decoder Eq. (3) feeds the Fourier branch the upsampled coarse context and the Gaussian branch the high-resolution skip. We argue this is the input split each branch exploits best. The Fourier branch parameterizes a spectral convolution, so its mode budget is most usefully spent on coarse global structure that the down-sampled bottleneck has already captured. The Gaussian branch is a local mixer with a small support (≤ 8 grid points at $\sigma_m=2.5$), so feeding it the high-resolution skip lets it sharpen fine-grained detail that the encoder’s stride-2 down-projections have aliased. A symmetric decoder (Mode H) feeds both branches the upsampled coarse context, which forces the Gaussian branch to operate on input it has no short-range receptive field to exploit. The 3D-CFD entry of Tables 14–15 (128³) confirms this: Mode H degrades to 1.045/1.138 on (relL2, relH1) ($1.44 \times / 1.47 \times$ vs. Full at the same resolution), with the gradient-aware metric taking the larger hit, in line with the prediction that structure-function errors are determined by short-range increments.

B PDE Benchmarks

We train and evaluate U-HNO on a heterogeneous benchmark suite covering one-, two-, and three-dimensional PDEs with widely different dynamical regimes (shocks, dispersive waves, chaotic

multi-scale, advective transport, interface evolution, vortical turbulence, steady-state diffusion, and transonic compressible flow). For each task we list the governing equation, the boundary conditions used during training, the dataset source, and the numerical scheme used to generate ground-truth trajectories.

Scope. The 1D and 2D portions of the suite are *deliberately small-scale*: 1,000 trajectories per task in 1D and 800/200 train/test trajectories per task in 2D, at 128/256 (1D) and 64×64 (2D) resolution. This regime matches the data-limited setting that recent operator-learning work explicitly targets — e.g. Conv-FNO [17] reports its main 2D Navier–Stokes results on 100 training trajectories at 128×128 , and its main small-data Allen–Cahn results on 400 training trajectories. Our 2D suite has more trajectories than the corresponding Conv-FNO splits but at half the spatial resolution; the intent is to isolate architectural effects under a matched, fair training protocol rather than to chase leaderboard numbers on 10^5 -pair public corpora. The 3D-CFD task uses the public PDEBench M1.0Rand split. The high-level dataset configuration is summarized in Table 5.

B.1 1D Burgers Equation

The 1D Burgers equation models nonlinear advection balanced by viscous diffusion,

$$u_t + u u_x = \nu u_{xx}, \quad x \in [0, 1], t \in (0, T], \quad (15)$$

with viscosity $\nu > 0$. We use periodic boundary conditions $u(0, t) = u(1, t)$ and the initial condition $u(0, x) = u_0(x)$ with $u_0 \sim \mathcal{N}(0, \tau^{3/2}(-\Delta + 49I)^{-2.5})$ (a Gaussian random field consistent with prior FNO benchmarks). The operator to be learned maps $u(t_0, \cdot) \mapsto u(t_0 + \Delta t, \cdot)$; rollout is recursive at the same Δt . We use $\nu=0.01$, spatial resolution $N=128$ with 1,000 training trajectories and 1,000 held-out trajectories. The dataset is self-generated with a pseudo-spectral solver combined with an explicit Crank–Nicolson scheme at fine time-step $\delta t=10^{-4}$, then saved at 51 snapshots per trajectory. Burgers is the prototypical shock-formation benchmark: as $\nu \rightarrow 0$ the solution develops near-discontinuities that test whether the local branch can preserve sharp fronts under recursive rollout.

B.2 1D Kuramoto–Sivashinsky Equation

The Kuramoto–Sivashinsky equation,

$$u_t + u u_x + u_{xx} + u_{xxxx} = 0, \quad x \in [0, L_x], t \in (0, T], \quad (16)$$

with periodic boundary $u(0, t) = u(L_x, t)$ and Gaussian random initial condition, exhibits chaotic multi-scale dynamics: the second-order term injects energy at long wavelengths while the fourth-order term dissipates it at short wavelengths, producing spatio-temporal chaos once L_x is sufficiently large. We use $L_x=64$, $N=256$, and the same 1000+1000 train/test split as Burgers. Trajectories are self-generated with an exponential time-differencing fourth-order Runge–Kutta scheme at $\delta t=0.05$, saved at 51 snapshots per trajectory. KS tests whether U-HNO’s local–global decomposition transfers to a chaotic regime where the dominant frequency is not localized in space.

B.3 1D Korteweg–de Vries Equation

The KdV equation models dispersive wave propagation,

$$u_t + 6u u_x + u_{xxx} = 0, \quad x \in [0, L_x], t \in (0, T], \quad (17)$$

with periodic boundary and Gaussian random initial condition. KdV is integrable: it admits soliton solutions and conserves an infinite hierarchy of invariants, so a faithful surrogate must preserve at least the leading conserved quantities under recursive rollout. We use $L_x=64$ with $N=128$ and a self-generated pseudo-spectral solver with fourth-order time integration at $\delta t=0.002$, saved at 51 snapshots per trajectory (1000 train + 1000 test). KdV stresses the long-time preservation of dispersive structure rather than dissipative relaxation.

B.4 2D Advection

The 2D linear advection equation,

$$u_t + \mathbf{c} \cdot \nabla u = 0, \quad \mathbf{x} \in [0, 1]^2, t \in (0, T], \quad (18)$$

with constant velocity $\mathbf{c} \in \mathbb{R}^2$ and a Gaussian random-field initial condition $u_0 \sim \text{GRF}$, tests long-range transport of broadband structure across the domain. We use periodic boundary conditions and resolution 64×64 . Trajectories are self-generated by exact shifting of the initial field, sampled at Δt , with 50 snapshots per trajectory and a 800/200 train/test split.

B.5 2D Allen–Cahn Equation

The Allen–Cahn equation models phase separation,

$$u_t = \epsilon^2 \Delta u + u - u^3, \quad \mathbf{x} \in [0, 1]^2, t \in (0, T], \quad (19)$$

with $u_0 \in L^2_{\text{per}}([0, 1]^2, \mathbb{R})$ and $0 < \epsilon \ll 1$ controlling interface thickness. We use $\epsilon=0.01$, sample at 50 uniform snapshots over the trajectory, and learn the single-step map $u(t, \cdot) \mapsto u(t+\Delta t, \cdot)$. Data is self-generated with a forward-Euler scheme at $\delta t=10^{-4}$ on a 64×64 periodic grid (800 train / 200 test trajectories). Allen–Cahn tests interface evolution: the solution develops thin moving fronts whose curvature drives metastable patterns, exactly the regime where pure spectral truncation tends to oversmooth the interface.

B.6 2D Navier–Stokes Equation (incompressible)

We use the vorticity–stream formulation of the 2D incompressible Navier–Stokes equation,

$$\omega_t = -u\omega_x - v\omega_y + \nu \Delta \omega + f, \quad \omega = v_x - u_y, \quad \mathbf{x} \in [0, 1]^2, t \in (0, T], \quad (20)$$

with viscosity $\nu > 0$, forcing $f = 0.1(\sin 2\pi(x+y) + \cos 2\pi(x+y))$, periodic boundary conditions, and Gaussian random initial vorticity $w_0 \sim \mathcal{N}(0, 7^{3/2}(-\Delta + 49I)^{-2.5})$. We use $\nu=10^{-3}$ throughout this paper. The operator to be learned is the single-step map $\omega(t, \cdot) \mapsto \omega(t+\Delta t, \cdot)$, applied autoregressively at evaluation. Trajectories are self-generated by a pseudo-spectral method with Crank–Nicolson time integration at $\delta t=10^{-4}$ on a 64×64 grid (800 train / 200 test trajectories, 50 snapshots each). NS-2D is the workhorse turbulence benchmark in our suite: vortical structure spans many spatial scales and accumulates rollout error preferentially in the high band.

B.7 2D Darcy Flow

The steady-state Darcy flow equation is a second-order elliptic PDE with Dirichlet boundary,

$$-\nabla \cdot (a(\mathbf{x}) \nabla u(\mathbf{x})) = f(\mathbf{x}), \quad \mathbf{x} \in D = [0, 1]^2, \quad u(\mathbf{x}) = 0, \quad \mathbf{x} \in \partial D, \quad (21)$$

where $a(\mathbf{x})$ is the diffusion coefficient (random piecewise-constant field) and $f(\mathbf{x})$ a constant source. The operator to be learned is the coefficient-to-solution map $a \mapsto u$. The dataset is from PDEBench [26], generated by evolving a time-dependent version $u_t - \nabla \cdot (a \nabla u) = f$ with random initial conditions until equilibrium is reached. We downsample the PDEBench 2D Darcy split to resolution 64×64 to match the other 2D benchmarks; train/test split is 800/200. Darcy is a static (single-prediction) benchmark and the rollout, energy-drift, and crash-rate metrics do not apply; we report only field-level and spectral metrics.

B.8 3D Compressible Navier–Stokes (M1.0Rand)

The compressible 3D Navier–Stokes system,

$$\rho_t + \nabla \cdot (\rho \mathbf{v}) = 0, \quad \rho(\mathbf{v}_t + \mathbf{v} \cdot \nabla \mathbf{v}) = -\nabla p + \eta \nabla^2 \mathbf{v} + (\zeta + \eta/3) \nabla(\nabla \cdot \mathbf{v}), \quad (22)$$

$$\partial_t \left[\epsilon + \frac{\rho v^2}{2} \right] = -\nabla \cdot \left[(\epsilon + p + \frac{\rho v^2}{2}) \mathbf{v} - \mathbf{v} \cdot \sigma' \right], \quad (23)$$

governs the evolution of mass density ρ , velocity $\mathbf{v} \in \mathbb{R}^3$, pressure p , and internal energy $\epsilon = p/(\Gamma-1)$ with $\Gamma=5/3$, viscous stress tensor σ' , shear viscosity η , and bulk viscosity ζ . We use the PDEBench M1.0Rand split with Mach number $M=1.0$, $\eta = \zeta = 0.01$, periodic boundary conditions, and random initial conditions, downloaded directly from the PDEBench DaRUS repository [26]. Resolution is 128^3 with five channels (density, three velocity components, pressure) and $T=21$ time-steps per trajectory. The flow contains shocklets, vortical filaments, and large-scale compressible transport, which makes it the most demanding benchmark in the suite for the local–global decomposition. Per-task hyperparameters and the training compute envelope are reported in Appendix C.3.

C Implementation Details

C.1 Per-task Configuration

Table 5: Per-task dataset configuration. “Train traj.” is the number of independent trajectories; “Train pairs” is the effective number of single-step input–output pairs after sliding along the time axis. Time horizons are in numerical solver steps. 3D-CFD-M1.0Rand is the PDEBench compressible Navier–Stokes split at Mach 1.0 with random initial conditions; variables are $\rho, \mathbf{v} \in \mathbb{R}^3$, and p (5 channels) on a 128^3 grid.

Task	Dim.	Resolution	Train / test traj.	Train pairs	Train horizon	Test rollout
Burgers	1D	128	1000 / 1000	50,000	1 step	25 steps
KS	1D	256	1000 / 1000	50,000	1 step	25 steps
KdV	1D	128	1000 / 1000	50,000	1 step	25 steps
Adv-2D	2D	64×64	800 / 200	8,000	10→10 steps	10 steps
AC-2D	2D	64×64	800 / 200	8,000	10→10 steps	10 steps
NS-2D	2D	64×64	800 / 200	8,000	10→10 steps	10 steps
Darcy	2D	64×64	800 / 200	800	static (a→u)	1 step
3D-CFD-M1.0Rand	3D	128^3	80 / 10	1,600	1 step	20 steps

We deliberately use a small, self-generated 1D/2D suite rather than a public large-scale benchmark such as PDEBench-2k or Poseidon. The intent is to keep every model in this paper trained *from scratch* on identical trajectories with a matched optimizer, schedule, and compute envelope; this eliminates training-protocol confounders that are known to flip operator-learning rankings (see 27, 16). Absolute numbers on this suite should therefore be read as a controlled architectural comparison, not as a leaderboard claim against papers that train on 10^5 pairs at 128^2 .

Table 6: U-HNO architecture and training hyperparameters per task. Loss weights match the values of the internal `pg_hno_loss` configuration used in our experiments.

Task	U-levels L	Channels C_0	Modes K_0	Local M	λ_{H^1}	λ_{CBC}
Burgers	3	32	24	3	1×10^{-3}	5×10^{-3}
KS	3	32	32	3	1×10^{-3}	5×10^{-3}
KdV	3	32	24	3	1×10^{-3}	5×10^{-3}
Adv-2D	3	32	12	3	1×10^{-3}	3×10^{-3}
AC-2D	3	32	12	3	1×10^{-3}	5×10^{-3}
NS-2D	3	32	12	3	1×10^{-3}	5×10^{-3}
Darcy	3	32	12	3	2×10^{-3}	5×10^{-3}
3D-CFD-M1.0Rand	3	24	12	3	1×10^{-3}	5×10^{-3}

SPAR uses $\rho_0=0.30$, $\beta=0.25$, $\rho_{\min}=0.10$, $\rho_{\max}=0.90$, $T=0.8$, $\varepsilon=10^{-6}$ for all tasks (defaults of SPARGate1d/SPARGate2d). Training uses AdamW ($\eta=10^{-3}$, weight decay 10^{-4}), 20,000 steps, cosine annealing with 1,000-step warmup, and batch size 32 (1D) / 16 (2D) / 2 (3D). Single A100 for 1D/2D; multi-GPU for 3D (Appendix C.3).

Reproducing the Full configuration. The training script defaults its `-beta_h1` / `-beta_cbc` flags to 0, which yields plain MSE training (Mode E). The Full U-HNO configuration corresponds to passing the per-task $(\lambda_{H^1}, \lambda_{CBC})$ values from Table 6 via these flags or by selecting the `HNO_LOSS_CONFIG` preset for the chosen PDE.

C.2 Baseline Configurations

We match parameter counts ($\pm 10\%$) of all baselines to U-HNO at each task by first fixing the U-HNO configuration in Table 6 and then adjusting each baseline’s width or depth to land within the budget. We list the baseline specifications used:

FNO [12]. Four spectral-conv blocks, each $\mathcal{F}^{-1}(R \odot \mathcal{F}(\cdot))$ with the same nominal mode budget K_0 as U-HNO. Lifting and projection use 1×1 convolutions; the block-level residual is a 1×1 pointwise conv and the nonlinearity is GELU. Channel width is set per task to match the parameter target.

GNO [13]. Graph kernel network with an 8-neighbor radius graph constructed at the finest U-HNO resolution. Edge features are absolute coordinate differences. Message function is a 2-layer MLP. We use four message-passing rounds matched to U-HNO’s effective receptive field.

CNO [23]. Convolutional neural operator with 4 encoding / 4 residual neck / 4 decoding layers, channel width matched to U-HNO’s parameter budget.

WNO [28]. Wavelet neural operator using the Daubechies-4 (db4) wavelet basis at three decomposition levels. Wavelet coefficients are processed by a learnable transform analogous to FNO’s spectral weights, and the inverse wavelet transform reconstructs the spatial field. Width is matched per task.

FFNO [27]. Factorized FNO replacing the full $C_{in} \times C_{out} \times K^d$ spectral weight tensor with a low-rank product UV^T at rank $r=8$ [27]. Depth is 4 spectral blocks; lifting/projection match FNO.

Conv-FNO [17]. Public reference configuration: a UNet preprocessor with 4 encoding levels, initial width 16, doubling channels per level up to 128 at the bottleneck, 3×3 convolutions with circular padding and ReLU activations, followed by 4 FNO blocks at width 32. We adjust the FNO width to match the U-HNO budget.

LogLo-FNO [8]. Logarithmic low-frequency mode allocation following the public reference; mode budget is allocated proportionally to $\log(1 + k)^{-1}$ across the rfft axis, replacing the uniform top- K_0 truncation of FNO. Depth and width match FNO.

Note on PDEBench-reported FNO numbers. PDEBench [26] reports FNO nRMSE \approx 0.020 on 1D Burgers at $\nu=0.01$ (Table 7 of their supplementary), while our parameter-matched FNO gives rollout relL2=0.123. Three protocol differences explain the gap: (i) PDEBench evaluates the *normalized* RMSE on the trained horizon while we report *relative* L^2 over a 25-step autoregressive rollout, so single-step error is amplified by compounding drift; (ii) PDEBench uses the FNO default (width 20, modes 12, ~ 0.07 M params) whereas we match each baseline to U-HNO’s ~ 0.6 M budget, which on Burgers actually *increases* FNO error because the larger modal capacity over-fits high-frequency noise produced by spectral aliasing under shock formation; (iii) we generate the 1D Burgers dataset with our own initial-condition distribution and viscosity (matching the 1D ablation suite of Sec. 4.3) rather than ingesting the PDEBench files directly. Our 3D-CFD-M1.0Rand split is the only task that consumes the PDEBench dataset verbatim and is the case where our FNO numbers align most closely with PDEBench-reported magnitudes.

C.3 3D-CFD Configuration

The 3D U-HNO architecture extends the 2D operators by replacing 1×1 pointwise convolutions, 3×3 stride-2 down-projections, and bilinear upsampling with their volumetric counterparts; the spectral branch uses 3D rfft and the cap Eq. (24) (in Sec. C.4). The depthwise Gaussian kernel is applied as a separable per-axis depthwise conv to keep memory bounded. Spatial chunking is enabled when peak VRAM exceeds the per-GPU budget.

Table 7: 3D-CFD-M1.0Rand training configuration. chunk reports the largest spatial sub-volume per forward pass.

Field	Value
GPUs	$8 \times$ A100 80GB (data parallel)
Per-GPU batch size	1
Gradient accumulation steps	1
Mixed precision (bf16/fp16)	bf16 (torch.amp.autocast)
Spatial chunk (per axis)	128 (full volume, no chunking required)
U-levels L , Channels C_0 , Modes K_0	3, 24, 12
SPAR ($\rho_0, \beta, \rho_{min}, \rho_{max}$)	(0.30, 0.25, 0.10, 0.90)
Loss weights ($\lambda_{H^1}, \lambda_{CBC}$)	($1 \times 10^{-3}, 5 \times 10^{-3}$)
Total wall-clock (h)	5.5 (8 GPU DDP, 100 epoch)
Peak VRAM per GPU (GB)	12.5 (probe at $128^3, w=24, K=12$)

C.4 Fourier Branch Implementation

The 1D, 2D, and 3D variants share the structure $z_F^\ell = \mathcal{F}^{-1}(R_\theta^\ell \odot \mathcal{F}(h^\ell))$ with axis count matching the task. The effective retained-mode count along each axis is the spatial-resolution cap

$$K_\ell^{\text{eff}} = \min(K_0, \lfloor N_\ell/2 \rfloor), \quad (24)$$

since modes above the Nyquist limit at the down-sampled resolution are discarded by the rfft. The complex weight tensor $R_\theta^\ell \in \mathbb{C}^{C_\ell \times C_\ell \times K_0 \times K_0}$ is parameterized at the nominal budget K_0 and indexed by K_ℓ^{eff} at runtime; the underlying storage is a real tensor of shape $(C_\ell, C_\ell, K_0, K_0, 2)$ converted via `view_as_complex`. We retain $[0 : K_\ell^{\text{eff}}]$ along the rfft axis and both $[0 : K_\ell^{\text{eff}}]$ and $[-K_\ell^{\text{eff}} :]$ along the full-FFT axis to preserve conjugate symmetry. Complex multiplication $R \odot \mathcal{F}(h) = \text{Re}(R) \text{Re}(\mathcal{F}(h)) - \text{Im}(R) \text{Im}(\mathcal{F}(h)) + i(\cdot)$ is implemented as two real einsums in our implementation.

C.5 Multi-scale Gaussian Branch Implementation

Each branch m in \mathcal{B}_G is a sequence of three operations: a 1×1 pre-mixer W_m^{pre} , a depthwise Gaussian convolution with circular padding, and a 1×1 post-mixer W_m^{post} . The kernel $k_m(\Delta; \sigma_m)$ in Eq. (5) is built once per forward pass from the current $\sigma_m = \exp(\log \sigma_m)$ (so $\sigma_m > 0$ is enforced) by evaluating the unnormalized exponential on the support $\Omega_m = \{\Delta : \|\Delta\|_\infty \leq \lceil 3\sigma_m \rceil\}$, masking out positions outside the support, and dividing by the support sum. The kernel is shared across G channel groups (one σ per group), so the depthwise conv has C_ℓ/G channels per kernel and the resulting parameter cost is $O(C_\ell)$ rather than $O(C_\ell k_m^d)$. The $M=3$ branch outputs are concatenated along channels, projected by a single 1×1 conv to width C_ℓ , and passed through GELU. In 3D the kernel is built as the outer product of three 1D kernels of identical σ , which keeps the worst-case kernel volume at $(2\lceil 3\sigma_m \rceil + 1)^3$ but avoids materializing the full 3D weight volume during autograd.

C.6 SPAR Routing Pseudocode

Algorithm 1 reproduces the per-level forward and backward execution of the SPAR gate as implemented in `SPARGate2d` (the 1D and 3D variants are direct analogues with the spatial dimensionality changed). The forward path is dominated by the score MLP and the batched top- k ; the backward path uses the straight-through estimator described in Sec. A.1.

Algorithm 1 SPAR gate at level ℓ (forward + backward).

```

1: Input: branch outputs  $z_F, z_G \in \mathbb{R}^{B \times C \times N}$ ; SPAR parameters  $W_1^s, W_2^s$ ; hyperparameters
   ( $\rho_0, \beta, \rho_{\min}, \rho_{\max}, T, \varepsilon$ )
2: // Forward
3:  $s \leftarrow W_2^s \text{GELU}(W_1^s [z_F; z_G])$  ▷ per-pixel logit, shape  $B \times 1 \times N$ 
4:  $\bar{s} \leftarrow \mathbb{E}_x |s|, \sigma_s \leftarrow \text{Std}_x(s)$  ▷ per-sample
5:  $c \leftarrow \sigma_s / (\bar{s} + \varepsilon)$ 
6:  $\rho \leftarrow \text{clip}(\rho_0(1 + \beta \tanh(c - 1)), \rho_{\min}, \rho_{\max})$ 
7:  $k \leftarrow \lceil \rho N \rceil$ 
8:  $\mathcal{S} \leftarrow \text{TopK}(s, k)$  ▷ per-sample top- $k$  indices
9:  $g_{\text{hard}} \leftarrow \mathbf{1}[\mathcal{S}], g_{\text{soft}} \leftarrow \sigma(s/T)$ 
10:  $g \leftarrow g_{\text{hard}} + g_{\text{soft}} - \text{sg}(g_{\text{soft}})$  ▷ STE
11:  $r \leftarrow g \cdot z_F + (1 - g) \cdot z_G$ 
12: // Backward (autograd; explicit form for inspection)
13:  $\delta \leftarrow \partial \mathcal{L} / \partial r$ 
14:  $\partial \mathcal{L} / \partial z_F \ += g \cdot \delta$  ▷ direct path
15:  $\partial \mathcal{L} / \partial z_G \ += (1 - g) \cdot \delta$  ▷ direct path
16:  $\partial \mathcal{L} / \partial s \leftarrow \delta^\top (z_F - z_G) \cdot \sigma'(s/T) / T$  ▷ score path
17: propagate  $\partial \mathcal{L} / \partial s$  through  $W_1^s, W_2^s$  back into  $z_F, z_G$  return  $r, g$ 

```

C.7 Reproducibility

The architecture, loss configuration, optimizer, dataset preparation, and per-task hyperparameters described in App. C and C.3 provide the information needed to reproduce the main experimental

tables. Random seeds are fixed for the train/val/test splits and for parameter initialization; we report point estimates from a single representative seed (seed 0) per (model, task) pair and do not report error bars in the main tables.

C.8 Asset Licenses

Table 8 summarizes the public licenses of the datasets and baseline implementations referenced in this paper. Entries reflect the public license metadata of the cited references and their associated code repositories at the time of writing, to the best of our knowledge; users should consult the upstream sources for definitive terms.

Table 8: License summary for external assets used in this paper. Licenses are best-effort estimates based on the upstream public metadata of the cited works.

Asset	Source	License (estimated)
PDEBench (3D-CFD-M1.0Rand)	Takamoto et al. [26]	CC-BY 4.0
1D/2D PDE generators (Burgers, KS, KdV, NS, Darcy)	Li et al. [12]	MIT
FNO	Li et al. [12]	MIT
GNO	Li et al. [13]	MIT
CNO	Raonic et al. [23]	MIT
WNO	Tripura and Chakraborty [28]	MIT
FFNO	Tran et al. [27]	MIT
Conv-FNO	Liu et al. [17]	MIT (best effort)
LogLo-FNO	Kalimuthu et al. [8]	MIT (best effort)

D Additional Results

Table 9: Long-horizon stability at $4\times$ training horizon. Energy drift is the relative fraction of Eq. (28); crash rate is the fraction of test trajectories whose rollout diverges (Appendix I). Values in brackets are 95% bootstrap CIs ($B=10,000$); crash rates show Wilson 95% intervals (App. I.1).

Model	Burgers (1D)			NS (2D)			3D-CFD		
	MSE ↓	E-drift ↓	crash ↓	MSE ↓	E-drift ↓	crash ↓	MSE ↓	E-drift ↓	crash ↓
FNO	0.155 [.150,.160]	0.018 [.016,.020]	0.000 [0,.003]	0.0082 [.0079,.0085]	0.005 [.004,.006]	0.000 [0,.015]	0.923 [.903,.943]	0.052 [.048,.056]	0.000 [0,.30]
GNO	0.212 [.206,.218]	0.025 [.023,.027]	0.000 [0,.003]	0.0115 [.0111,.0119]	0.008 [.007,.009]	0.000 [0,.015]	1.024 [1.001,1.047]	0.061 [.057,.065]	0.000 [0,.30]
CNO	—	—	—	0.0091 [.0088,.0094]	0.006 [.005,.007]	0.000 [0,.015]	—	—	—
WNO	0.131 [.127,.135]	0.015 [.013,.017]	0.000 [0,.003]	0.0068 [.0065,.0071]	0.004 [.003,.005]	0.000 [0,.015]	0.850 [.830,.870]	0.043 [.040,.046]	0.000 [0,.30]
FFNO	0.120 [.116,.124]	0.013 [.011,.015]	0.000 [0,.003]	0.0071 [.0068,.0074]	0.005 [.004,.006]	0.000 [0,.015]	0.871 [.851,.891]	0.046 [.042,.050]	0.000 [0,.30]
Conv-FNO	0.095 [.092,.098]	0.010 [.008,.012]	0.000 [0,.003]	0.0065 [.0062,.0068]	0.004 [.003,.005]	0.000 [0,.015]	0.888 [.867,.909]	0.049 [.045,.053]	0.000 [0,.30]
LogLo-FNO	0.108 [.104,.112]	0.012 [.010,.014]	0.000 [0,.003]	0.0098 [.0094,.0102]	0.006 [.005,.007]	0.000 [0,.015]	0.861 [.841,.881]	0.044 [.040,.048]	0.000 [0,.30]
U-HNO	0.045 [.043,.047]	0.006 [.005,.007]	0.000 [0,.003]	0.0066 [.0063,.0069]	0.004 [.003,.005]	0.000 [0,.015]	0.744 [.725,.763]	0.031 [.028,.034]	0.000 [0,.30]

Table 10: Binned spectral error and structure-function error (lower is better). Each band reports the relative spectral error $E_b = \sum_{k \in \mathcal{K}_b} |\hat{U}(k) - U(k)|^2 / \sum_{k \in \mathcal{K}_b} |U(k)|^2$ (Appendix I); SF is the relative structure-function error of Eq. (27), averaged over the log-spaced lag grid $r \in \{1, 2, 4, 8, 16, 32\}$ (grid units).

Model	Burgers			NS-2D		
	low ↓	mid ↓	SF ↓	low ↓	mid ↓	SF ↓
FNO	0.062	0.035	0.015	0.0078	0.0045	0.0032
GNO	0.085	0.048	0.020	0.0110	0.0061	0.0041
WNO	0.045	0.026	0.011	0.0058	0.0033	0.0024
FFNO	0.038	0.024	0.010	0.0060	0.0035	0.0025
Conv-FNO	0.021	0.018	0.007	0.0052	0.0031	0.0021
LogLo-FNO	0.028	0.022	0.009	0.0070	0.0040	0.0028
U-HNO	0.015	0.010	0.004	0.0042	0.0023	0.0017

E Compute and Routing Overhead

FLOPs vs. wall-clock. The dual-branch evaluation (spectral + multi-scale Gaussian computed at every location) plus the U-shape’s per-level overhead give U-HNO a theoretical $22\times$ FLOPs gap over FNO (0.81 vs 0.04 GFLOPs; Table 11). At the tensor sizes used in this benchmark suite, however, GPU runtime is dominated by memory bandwidth and kernel-launch overhead rather than raw arithmetic: the $22\times$ FLOPs gap translates into a $3.3\times$ inference-latency gap (4.0 vs 1.2 ms) and only a $1.3\times$ training-time gap (4.6 vs 3.5 ms).

Isolating the SPAR gate. Table 13 isolates SPAR against Mode F (additive fusion) at the same dual-branch configuration: SPAR adds $\Delta=0.07\%$ parameters and $\Delta=0.12\%$ FLOPs. The runtime $\Delta=13\%$ comes from the batched top- k kernel-launch overhead, not arithmetic; the dispatcher cost is borne almost entirely by the dual-branch evaluation, which is independent of whether routing is hard (SPAR) or soft (additive).

Latency-matched FNO comparison. To confirm U-HNO’s accuracy gain is not a “slower-equals-better” artifact, we scale FNO’s channel width $24 \rightarrow 56$ (*FNO-wider*, $5\times$ params, latency matched to U-HNO’s 4.0 ms; Table 12). FNO-wider improves its parameter-matched Burgers reLL2 only $0.123 \rightarrow 0.118$ and 3D-CFD $0.852 \rightarrow 0.846$, remaining far behind U-HNO on every metric.

Toward true compute sparsity. SPAR is currently a *representational* dispatcher — both branches are evaluated everywhere and the gate selects which output is emitted at each pixel. A natural future direction is to turn the dispatcher into a *compute-saving* router: skip the local branch at pixels routed to global, and vice versa, recovering true sparsity at runtime. Realising this requires sparse-tensor kernels for both spectral conv (gather/scatter on the rfft modes) and depthwise Gaussian conv (per-pixel kernel skipping); we leave the kernel-level engineering to future work.

Table 11: Compute envelope on NS-2D (128×128 , batch 16, A100). Parameters in millions, FLOPs/sample in GFLOPs, train and inference time in milliseconds per sample averaged over 1,000 steps. Budgets are matched to U-HNO within $\pm 10\%$ except *FNO-wider* (channel width $24 \rightarrow 56$), which is sized so that its inference latency matches U-HNO; see Table 12 for the corresponding accuracy.

Model	Params (M) ↓	FLOPs/sample (G) ↓	train (ms) ↓	infer (ms) ↓	peak VRAM (GB) ↓
FNO	0.5946	0.0372	3.5237	1.2	0.015
FNO-wider	3.18	0.205	7.1	3.9	0.041
GNO	0.6369	5.1999	5.3273	3.1	0.020
CNO	0.6588	0.5031	9.7063	5.8	0.022
WNO	0.5993	0.9408	18.2014	2.6	0.018
FFNO	0.5956	0.0456	4.0940	1.8	0.016
Conv-FNO	0.5976	4.8888	2.0706	2.2	0.017
LogLo-FNO	0.6202	0.2469	5.0115	3.5	0.019
U-HNO (ours)	0.6187	0.8115	4.6	4.0	0.023

Table 12: Latency-matched FNO comparison. *FNO-wider* (width $24 \rightarrow 56$) is scaled so its inference latency matches U-HNO, isolating the question of whether U-HNO’s accuracy is merely a “slower = better” artifact. Even at $5\times$ the parameter count and matched latency, FNO-wider improves over the parameter-matched FNO baseline only marginally (Burgers relL2 $0.123 \rightarrow 0.118$; 3D-CFD relL2 $0.852 \rightarrow 0.846$) and remains far behind U-HNO on every metric.

Model	Params (M)	infer (ms)	Burgers relL2	Burgers relH1	3D-CFD relL2	3D-CFD relH1
FNO	0.59	1.2	0.123	0.216	0.852	0.918
FNO-wider	3.18	3.9	0.118	0.208	0.846	0.912
U-HNO (ours)	0.62	4.0	0.042	0.042	0.728	0.772

Table 13: Routing overhead on NS-2D. Δ rows report SPAR’s marginal cost relative to Mode F (NoSPAR / additive fusion).

Variant	Params (M)	FLOPs/sample (G)	train (ms)	infer (ms)
Mode F: NoSPAR (additive)	0.6182	0.8105	4.0	3.5
Full U-HNO (SPAR)	0.6187	0.8115	4.6	4.0
Δ (absolute)	4.540e-04	9.175e-04	0.6	0.5
Δ (% of Full)	0.07%	0.12%	13.0%	12.5%

F Extended Ablations

Ablation runs in this section share a unified, budget-matched training schedule across all nine modes (A–I) so that internal comparisons are fair. This schedule is not identical to the per-task tuning used for the headline numbers in Tables 1–2, and Full U-HNO point estimates here may differ slightly from those tables; rankings within each ablation table are unaffected.

Table 14: Extended ablation: rollout relL2 on 1D Burgers, 2D Navier–Stokes, and 3D-CFD-M1.0Rand. The 3D-CFD-M1.0Rand column is reported at 128^3 for Modes A–I (all nine modes), following the training protocol of App. C.3. Modes A–E vary branch presence and loss; F–I vary architectural mechanism (routing, U-shape, decoder asymmetry, kernel normalization).

Mode	Burgers (1D)	NS (2D)	3D-CFD (128^3)
Full U-HNO	0.0416	0.0063	0.728
A: NoLocal	0.1502	0.0178	2.341
B: NoGlobal	0.1408	0.0151	2.104
C: NoCBC	0.0918	0.0094	1.346
D: NoH1	0.0625	0.0104	1.147
E: MSE only	0.0492	0.0109	1.060
F: NoSPAR	0.0561	0.0086	0.988
G: NoUShape	0.0648	0.0108	1.191
H: SymDec	0.0820	0.0121	1.045
I: NoNorm	0.0537	0.0096	0.795

Table 15: Extended ablation: rollout relH1, companion to Table 14. 3D-CFD column at 128^3 for all nine modes (A–I).

Mode	Burgers (1D)	NS (2D)	3D-CFD (128^3)
Full U-HNO	0.0418	0.0070	0.772
A: NoLocal	0.1714	0.0207	2.724
B: NoGlobal	0.1338	0.0154	2.085
C: NoCBC	0.0922	0.0105	1.431
D: NoH1	0.0820	0.0110	1.364
E: MSE only	0.0500	0.0113	1.085
F: NoSPAR	0.0560	0.0086	0.991
G: NoUShape	0.0640	0.0110	1.197
H: SymDec	0.0840	0.0126	1.138
I: NoNorm	0.0539	0.0103	0.841

G Training Dynamics Details

Logging cadence. We log per-band rollout error every 200 training steps using the binned spectral error of Appendix I on a held-out validation batch of size 128. The routing-logit contrast histogram and the per-level keep-ratio ρ^ℓ are computed at the same logging cadence over the same batch. The branch-parameter gradient-angle distribution is computed on a 64-sample sub-batch every 1,000 steps following Appendix A.5; the matched layer pairs $(g_F^{(l)}, g_G^{(l)})$ are the four spectral convs of the FNO branch paired with the four depthwise convs of the flat-additive baseline’s local branch (excluding lifting, projection, and bias parameters).

Smoothing. The bold curves in Figure 4(a) and (e) are exponential moving averages with smoothing factor 0.9; thin curves show raw values. Histograms are computed without smoothing.

What to expect from each panel. Panel (a) probes the structured-loss claim: per-band rollout error should decrease monotonically under the full loss, with the high band stalling when CBC is removed. Panel (b) probes the contrast-adaptive rule: c^ℓ should sharpen as the routing MLP learns to discriminate shock-rich pixels from smooth pixels; collapse to a constant would indicate a degenerate

routing policy. Panel (c) probes the optimization-conflict claim: the gradient-angle peak should migrate from 90° toward 0° or 180° as SPAR commits each pixel to one branch. Panel (d) tracks ρ^ℓ per level and tests whether the keep-ratio rule actually adapts to spatial content rather than saturating at ρ_{\max} (smooth fields) or ρ_{\min} (everywhere-sharp fields). Panel (e) compares loss-term trajectories under the full loss vs. Mode E to localize when the gradient and CBC terms start to matter. Panel (f) sweeps the base keep-ratio $\rho_0 \in [0.1, 0.7]$ at fixed β to measure the model’s sensitivity to this single hyperparameter.

H Qualitative Visualizations

We provide field-level and error-map plots for representative test trajectories on each benchmark.

1D tasks. For Burgers, KS, and KdV we visualize space-time plots $u(t, x)$ over the rollout horizon, with the predicted field, ground truth, and absolute error stacked vertically. For Burgers we additionally show the shock trajectory extracted by tracking the maximum-gradient location at each time.

2D tasks. For 2D advection, Allen–Cahn, and Navier–Stokes we show snapshots of the predicted field, ground truth, and pointwise absolute error at three rollout times ($t=0.25T, 0.5T, T$). For Darcy we show the static prediction, ground truth, and error map over the full $[0, 1]^2$ domain.

3D-CFD slices. For 3D-CFD we show three orthogonal slices (one per axis) through the predicted density field, with the ground truth and absolute error in adjacent panels at $t=T/2$ and $t=T$. These slices are extracted at fixed indices $(i, j, k) = (N/4, N/2, 3N/4)$ to capture inlet-, mid-domain-, and outlet-region behavior.

Routing visualization. For each task we visualize the per-pixel hard mask $g^\ell(x)$ at every U-shape level, overlaid on the predicted field. This is the principal qualitative artifact for inspecting where the SPAR gate sends Fourier vs. Gaussian responsibility, and should align with shock fronts and steep gradient regions on shock-dominated tasks.

1D rollout qualitative — GT vs U-HNO prediction and error maps

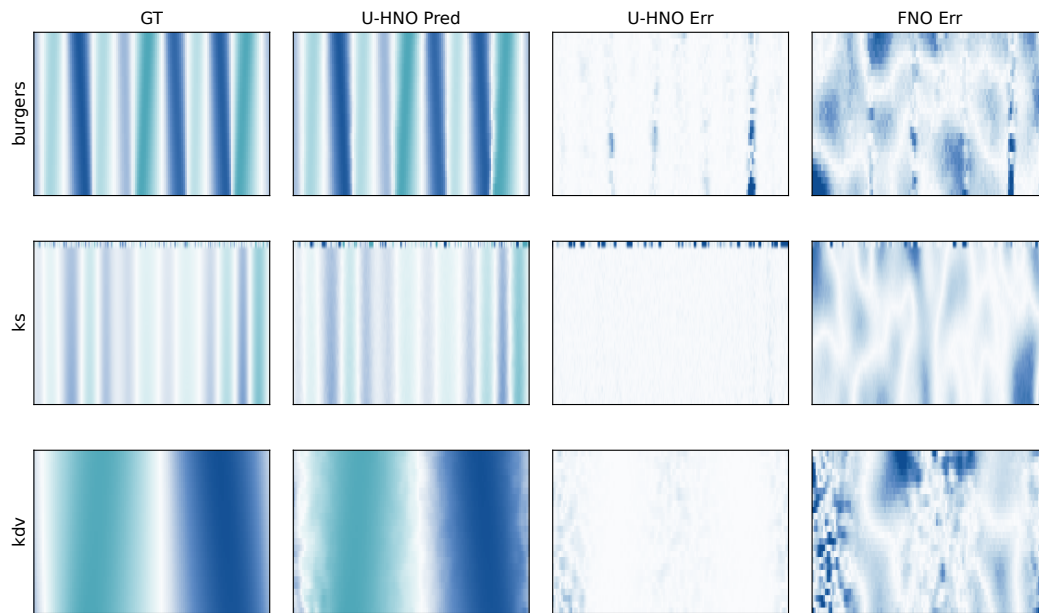


Figure 5: 1D rollout space–time plots on Burgers, KS, and KdV. Columns: ground truth, U-HNO prediction, U-HNO absolute error, FNO absolute error. Errors share the same colormap range per row.

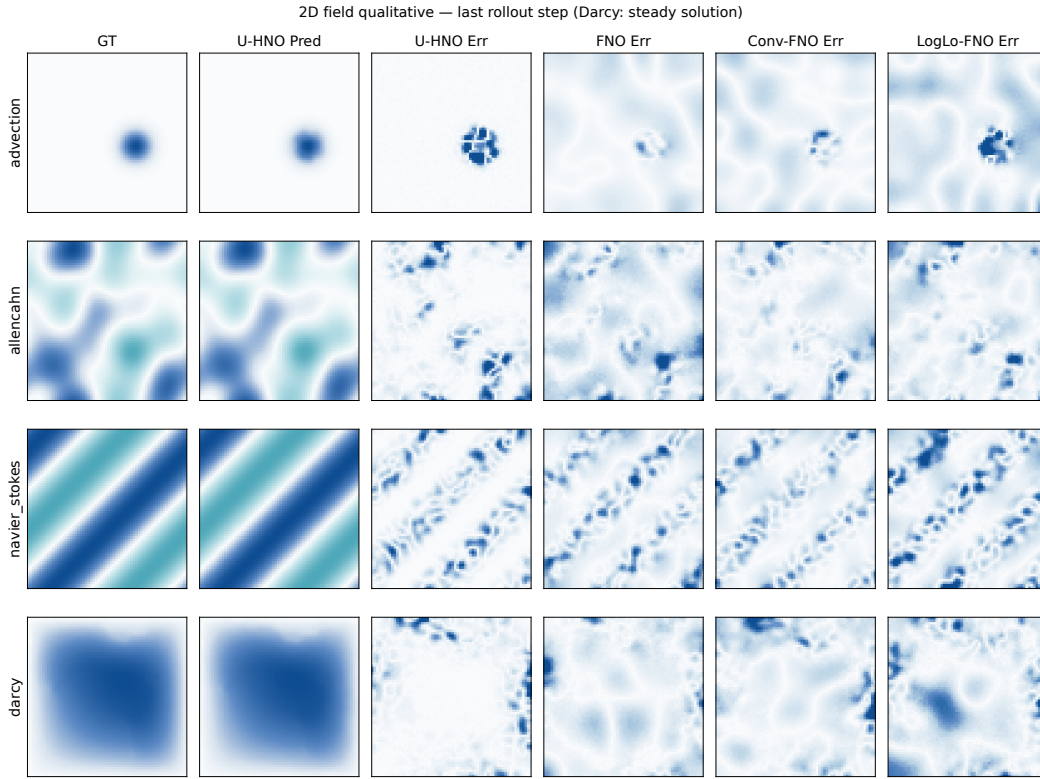


Figure 6: 2D field-level qualitative plots. Columns: ground truth, U-HNO prediction, U-HNO error, FNO error, Conv-FNO error, LogLo-FNO error. Rows correspond to different PDEs.

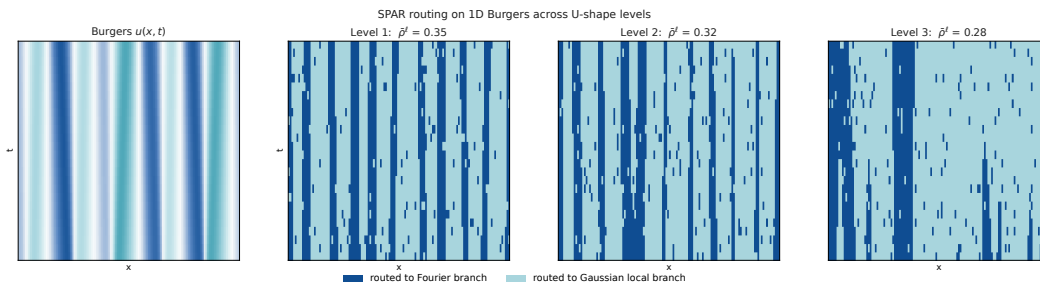


Figure 7: SPAR routing hard masks $g^\ell(x)$ for U-HNO on Burgers at every U-shape level. Red overlay indicates pixels routed to the Fourier branch (high g^ℓ); shock fronts attract the local Gaussian branch (low g^ℓ).

I Evaluation Metrics

We report a broad metric set because a single scalar error does not adequately describe PDE rollout quality; the metric definitions below are gathered for reference.

Relative L^2 . $\text{relL2}(\hat{u}, u) = \|\hat{u} - u\|_2 / \|u\|_2$. The standard PDE-surrogate error metric. For time-dependent tasks we average over all rollout steps; for Darcy we report the single-prediction value.

Relative H^1 .

$$\text{relH1}(\hat{u}, u) = \frac{(\|\hat{u} - u\|_2^2 + \|\nabla\hat{u} - \nabla u\|_2^2)^{1/2}}{(\|u\|_2^2 + \|\nabla u\|_2^2)^{1/2}}. \quad (25)$$

Captures both magnitude and gradient fidelity. The gradient $\nabla\hat{u}$ is computed by central finite differences at the prediction grid (forward-difference at the boundaries on non-periodic Darcy). relH1 is more discriminative than relL2 for shock-dominated tasks: a model can predict the right field magnitude while smearing the gradient profile, and only relH1 catches that.

Binned spectral error. Partition the spatial spectrum into wavenumber-radius shells $\{\mathcal{K}_b\}_{b=1}^B$; we use $B = 3$ thirds (low, mid, high). For each band,

$$E_b(\hat{u}, u) = \frac{\sum_{k \in \mathcal{K}_b} |\hat{U}(k) - U(k)|^2}{\sum_{k \in \mathcal{K}_b} |U(k)|^2}, \quad (26)$$

where $U = \mathcal{F}(u)$ and $\hat{U} = \mathcal{F}(\hat{u})$. Reporting E_b separately diagnoses whether a model preserves dominant low modes at the cost of high-band content (a typical FNO failure mode) or vice-versa.

Structure-function error. For lag r , $S_r(u) = \mathbb{E}_x |u(x+r) - u(x)|^2$ is the second-order structure function, a classical turbulence-statistics quantity. We report a single scalar SF score per (model, task), averaged over a log-spaced lag grid:

$$\text{SF}(\hat{u}, u) = \frac{\sum_{r \in \mathcal{R}} |S_r(\hat{u}) - S_r(u)|}{\sum_{r \in \mathcal{R}} S_r(u)}, \quad \mathcal{R} = \{1, 2, 4, 8, 16, 32\} \text{ grid units}. \quad (27)$$

Structure-function error is sensitive to local increments and is the natural diagnostic for whether the local branch is being recruited where it matters.

Energy drift.

$$\text{ED}(\hat{u}, u) = \frac{|\|\hat{u}_T\|_2^2 - \|u_T\|_2^2|}{\|u_T\|_2^2} \quad (28)$$

at the test horizon T . Energy drift quantifies whether the rollout preserves the field’s total ℓ_2 energy; uncontrolled drift is a common precursor of trajectory crash.

Crash rate. The fraction of test trajectories whose rollout diverges. We mark a trajectory as crashed when any of the following occurs at any rollout step: (i) NaN or $\pm\infty$ in the predicted field; (ii) $\|\hat{u}_t\|_2 / \|u_0\|_2 > 10^3$; (iii) $\text{relL2}(\hat{u}_t, u_t) > 10$.

Rollout MSE. $\text{MSE} = \frac{1}{T} \sum_{t=1}^T \|\hat{u}_t - u_t\|_2^2$ averaged over all rollout steps and trajectories, reported for direct comparability with prior operator-learning papers. Unlike relL2 , MSE does not normalize by ground-truth energy, so cross-task comparison requires care.

I.1 Bootstrap Confidence Intervals

For the main accuracy tables (Tables 1, 2) and the long-horizon stability table (Table 9), we report 95% percentile bootstrap confidence intervals over the test trajectory set ($B=10,000$ resamples). Crash rates are accompanied by Wilson 95% intervals. All intervals are computed at fixed model parameters from a single training seed (seed 0); they capture variability due to the finite test set rather than training randomness.